KONA Powder and Particle Journal

KONA Powder and Particle Journal No. 43 (2026) 22–46/https://doi.org/10.14356/kona.2026006 Review Paper

Experimental Methods for Model Parameters in the Discrete Element Method†

Fabian Krull, David Strohner and Sergiy Antonyuk*

Institute of Particle Process Engineering, University of Kaiserslautern-Landau (RPTU), Germany

The Discrete Element Method (DEM) is a widely used numerical method for studying, analyzing, and optimizing particulate processes. Based on contact models, DEM can predict the interactions of particles and particles with wall surfaces. Various contact models have been developed that consider various deformation and adhesion behaviors, particle shapes, and surface morphologies. However, accurate prediction of the real behavior requires experimental estimation and calibration of the model parameters for the studied particles. The objective of this paper is to provide a comprehensive overview of recent advancements in particle-property measurement methods, with a particular focus on the parameters of contact models. The measurement methods are classified into different categories, including static and dynamic loading and single particle and particle bed tests, with and without consideration of the surrounding liquid. A range of measurement techniques for estimating elastic and plastic properties, as well as friction and restitution coefficients in both air and liquid environments, are described, including nano- and tribo-indentation, compression, and impact tests. The applicability of these techniques was demonstrated using our own elastic–plastic model. The impacts of various influencing factors on material parameters and contact interactions are discussed. This overview can help identify suitable experimental techniques for calibrating and validating DEM models.

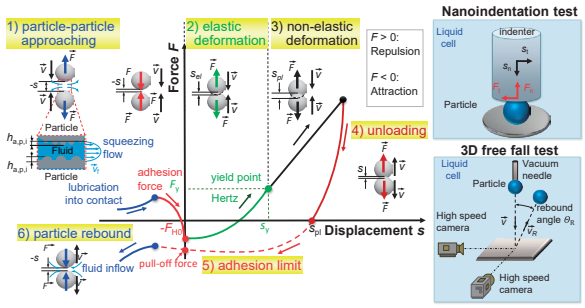

Keywords: particle, DEM, contact model, parameter estimation, nano/tribo-indentation, compression, impact, liquid

1. Introduction

The Discrete Element Method (DEM) is a widely employed approach for the analysis, description, and optimization of granular processes, such as milling (Burmeister et al., 2022; Tavares, 2017), silo discharging (Coetzee and Els, 2009; Hesse et al., 2020), coating (Grohn et al., 2023a; Suzzi et al., 2012), and powder segregation (Alizadeh et al., 2017; Guo et al., 2011; Hadi et al., 2024). Particle–particle and particle–wall interactions are described using contact models that consider a variety of particle characteristics depending on the specific particle material system (Luding, 2008). The coupling of the DEM with Computational Fluid Dynamics (CFD), as well as Lattice Boltzmann (LBM) or Smoothed Particle Hydrodynamics (SPH), allows the study of interactions with ambient fluids (Golshan et al., 2020; Potapov et al., 2001; Sakai et al., 2020), which extends the application to multiphase processes, such as filtration (Puderbach et al., 2021), fluidized bed (Breuninger et al., 2019; Deen et al., 2007; Di Maio and Di Renzo, 2007; Fries et al., 2011; Li et al., 2016), and granulation (Grohn et al., 2022b; Hayashi et al., 2020; Jajcevic et al., 2013). Three-phase systems consisting of liquid and gas as continuum phases with solid particles can be described by using a multiphase solver in CFD to consider the liquid–gas interactions (Vångö et al., 2018; Washino et al., 2023). In the case of wetted particle systems, such as pastes and agglomerates, the influence of liquid bridges can be described using bond models (Grohn et al., 2022a; Lian et al., 1998; Wu et al., 2018) or resolved simulations with the Immersed Boundary Method (Jain et al., 2012).

In order to achieve an accurate prediction of the real particle behavior in any particulate processes using DEM simulations, the experimental estimation or calibration of parameters and validation of contact models must be performed. Various standard tests have been established and implemented in DEM procedures to obtain particle parameters, such as compression tests, shear cell tests, static and dynamic angle of repose, and collision tests (Coetzee, 2017; Richter et al., 2020). Nevertheless, these tests are used to obtain parameters for dry particle systems. In a liquid environment, particle interactions such as friction and adhesion can differ from those in a dry system. Moreover, the lubrication forces can significantly influence the particle interactions and must be considered in the DEM, as well as in the unresolved CFD–DEM simulations. Therefore, novel test methods for measuring the DEM

† Received 28 June 2024; Accepted 25 October 2024
J-STAGE Advance published online 10 April 2025
* Corresponding author: Sergiy Antonyuk;
Add: Gottlieb-Daimler Street 44, 67663 Kaiserslautern, Germany
E-mail: sergiy.antonyuk@mv.rptu.de
TEL: +49-631-205-3524 FAX: +49-631-205-3055

parameters in liquid environments are necessary.

This review introduces the general interaction mechanisms of particles in liquids and the required parameters for contact models that can be applied in DEM to describe these contact interactions. The experimental methods used to obtain these parameters are summarized and explained in detail for dry particle systems and are also extended for ambient liquid and three-phase systems.

2. Discrete element method

The modeling of granular materials using DEM was first introduced by Cundall and Strack (1979). The particles are represented by spheres, and the walls are flat surfaces. The "soft" contact approach employs a physical force-displacement model to calculate the contact deformation as a virtual overlap of contact partners i and j. The position and translational velocity v_p of each particle with the mass m_p during time t are determined by numerically integrating Newton's second law (Zhu et al., 2007):

$$m_{P,i}\frac{dv_{P,i}}{dt} = F_{g,i} + \sum_{j=1}^{J} F_{c,i-j} + \sum_{k=1}^{K} F_{f,i,k} \quad (1)$$

where F_g and F_c describe the gravitational and contact forces. The last term on the right of **Eqn. (1)** includes fluid forces F_f acting on the particle from surrounding fluid like drag and pressure gradient forces.

The rotational movement of each particle with the angular velocity ω_p is described by Euler's equation:

$$J_{P,i}\frac{d\omega_{P,i}}{dt} = \sum_{j=1}^{J}\left(M_{t,ij} + M_{r,ij}\right) \quad (2)$$

including the moment of inertia J_p and all torques resulting from the tangential contact forces M_t and rolling friction M_r.

Since the behavior of granular materials is strongly influenced by the particle shape, e.g., flow (Giannis et al., 2023; Hesse et al., 2021), breakage (Zhang et al., 2020), and fluidization (Grohn et al., 2023b; Vollmari et al., 2016), the DEM has been extended using approaches for non-spherical particles (Kildashti et al., 2023; Lu et al., 2015). The most commonly used methods are the multi-sphere approach (Khazeni and Mansourpour, 2018; Kruggel-Emden et al., 2008a; Marigo and Stitt, 2015; Markauskas et al., 2010), superquadric (Cleary, 2004; Grohn et al., 2023b; Ji et al., 2020; Ma and Zhao, 2017; Soltanbeigi et al., 2018), and the bonded particle method (BPM) (Dosta et al., 2016; Park and Min, 2015; Rotter et al., 2023; Wolff et al., 2013) (**Fig. 1**).

The accurate calculation of contact forces and deformations in DEM is especially important for predicting the behavior of granular materials, which are significantly influenced by energy dissipation effects, such as plastic deformation, adhesion, and friction. To accommodate the diverse adhesion and deformation behaviors observed in various granular materials, several contact models have been developed.

2.1 Modeling of the contact force–displacement behavior

The interactions between two contact partners (two particles or a particle with a wall) approaching each other in a viscous fluid and coming into direct contact can be represented by the relationship between the total force F and the distance s between their surfaces ($s < 0$) or the contact displacement during their direct contact ($s \geq 0$) (**Fig. 2**). According to the direction of motion, the entire interaction can be divided into two successive phases: particle approach and separation. Contact forces can be classified into two categories: those that can act without direct contact, such as lubrication and adhesion forces, and those that arise from deformation during direct contact.

As the particles approach each other, the fluid is displaced from the contact zone, resulting in a lubrication or viscous repulsive effect. The force depends on the distance and approach speed and can be influenced by the rough microstructure of the surface. The minimum distance at which these forces act corresponds to the first direct contact between the largest asperities of both surfaces with the height $h_{a,p,i}$.

At a small distance between the surfaces of the particles, the adhesive forces increase, which can result in a notable attraction or tensile load on the particles. The viscous and adhesive forces determine the initial contact velocity of the

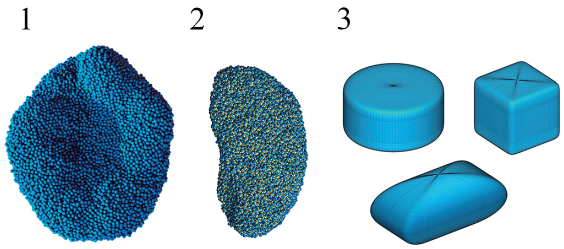

Fig. 1 Non-spherical particles in DEM: Bio-cell agglomerates using a multi-sphere approach **(1)** and BPM **(2)**. Different Superquadrics **(3)**.

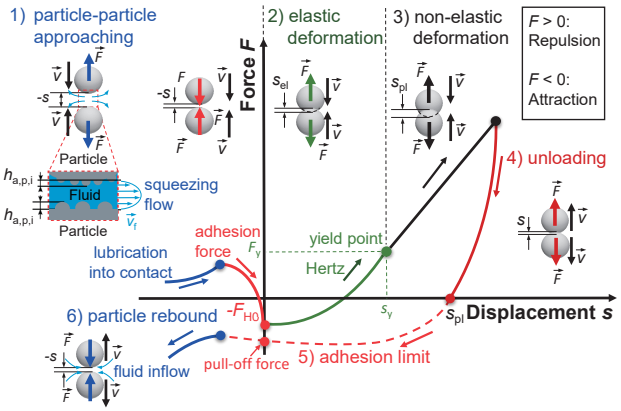

Fig. 2 Contact interactions between particles in a fluid.

particles, which can differ significantly from the undisturbed velocity. The direct contact of particles without any deformation is formed by the attractive adhesion force F_{H0} ("jump in"). As the particles continue to approach, elastic deformation begins. When the force–displacement curve intersects the abscissa, the total force equilibrium is obtained (total force equals zero). After this point, the compressive force first increases during elastic deformation, followed by plastic deformation after the yield point.

During unloading, the elastically stored deformation is recovered, and the force–displacement curve shows the permanent plastic deformation after complete unloading in the compression mode (s_{pl} at $F = 0$).

Particle separation can occur due to the residual stored elastic energy and is slowed down by the adhesive force, which increases during loading due to the formation of the plastic contact surface. When the unloading curve reaches the minimum, the so-called adhesion limit, the deformed contact surfaces separate as the distance increases. During separation, the fluid flows into the contact zone, creating lubrication forces that dissipate the kinetic energy of the rebound.

Different contact models have been developed to describe the various deformation behaviors of particles:

- *viscoelastic* (Brilliantov et al., 1996; Olsson and Jelagin, 2019; Schäfer et al., 1996; Stoianovici and Hurmuzlu, 1996; Tsuji et al., 1992; Ye and Zeng, 2017)
- *elastic–viscoplastic, plastic, and viscoplastic* (Adams et al., 2004; Walton and Braun, 1986; Weis et al., 2019)
- *plastic with adhesion* (Thornton and Ning, 1998; Weis et al., 2019)
- *elastic–plastic without adhesion* (Antonyuk et al., 2010; Johnson and Pollock, 1994; Thornton et al., 2017) and *with adhesion* (Hesse et al., 2023; Jasevičius et al., 2015; Olsson and Larsson, 2013; Pasha et al., 2014; Thakur et al., 2014; Tomas, 2007b)

The following studies provide an overview of contact models: Antonyuk, 2019; Kruggel-Emden et al., 2007; Kruggel-Emden et al., 2008b; Pöschel and Schwager, 2005; Stronge, 2010; Tomas, 2007b.

A significant limitation of the existing models is that they can only describe a single specific type of deformation. Furthermore, the parameters used in these models are not always based on directly measurable quantities; thus, they require adjustment. In the following section, a novel elastic–plastic contact model is presented, and its parameters are obtained for elastic–plastic dry (**Section 2.3.1**) and wet (**Section 3.3.5**) particles using the experimental techniques outlined in this study.

2.2 Elastic–plastic contact model

The contact model elucidates the transition from elastic to elastic–plastic deformation during loading. The analytical description of the force–displacement relationship is based on the pressure distribution in the actual contact area, which is derived from the Tomas model (Tomas, 2007a). The irreversible plastic deformation was obtained by solving the energy balance of the loading and unloading cycles. Contact consolidation due to plastic flattening was considered by calculating the following loading and unloading cycles and the increased adhesion force, which is described in detail in our previous studies (Hesse et al., 2023; Weis et al., 2019).

2.2.1 Elastic component of the force–displacement relationship

The elastic deformation can be described by the Hertz model (Hertz, 1882), which assumes an elliptical pressure distribution $p_{el}(r_c)$ in the elastically deformed contact area A_{el} with the radius $r_{c,el}$ (**Fig. 3**):

$$p_{el}(r_c) = p_{max}\sqrt{1-\left(\frac{r_c}{r_{c,el}}\right)^2} \tag{3}$$

and the maximum pressure p_{max} acting at the center of the contact area:

$$p_{max} = r_{c,el}\frac{2E^*}{\pi R^*} \tag{4}$$

which depends on the effective modulus of elasticity E^* and the radius of the contact surface curvature R^* given as

$$E^* = \left(\frac{1-\nu_i^2}{E_i}+\frac{1-\nu_j^2}{E_j}\right)^{-1} \tag{5}$$

$$R^* = \left(\frac{1}{R_i}+\frac{1}{R_j}\right)^{-1} \tag{6}$$

where ν is Poisson's ratio and R is the radius of the contact partners i and j.

The nonlinear relationship between elastic force F_{el} and displacement s was derived by Hertz by integrating the pressure over the contact area as follows:

$$F_{el} = \int_0^{r_{c,el}} p_{el}\cdot 2\pi r_c\,\mathrm{d}r_c = \frac{4}{3}E^*\sqrt{R^*\cdot s^3} \tag{7}$$

Due to the parabolic curvature of the force–displacement curve, the equivalent contact stiffness in **Eqn. (8)** increases during elastic deformation with the increase in the displacement and the equivalent radius of the contact surface curvature, such that larger particles behave more stiffly than smaller particles (Antonyuk et al., 2010):

$$k_{el}^* = \left(\frac{1}{k_i}+\frac{1}{k_j}\right)^{-1} = \frac{\mathrm{d}F_{el}}{\mathrm{d}s} = E^*\sqrt{R^*\cdot s} \tag{8}$$

The modulus of elasticity and Poisson's ratio are two material parameters that fully describe the elastic contact force.

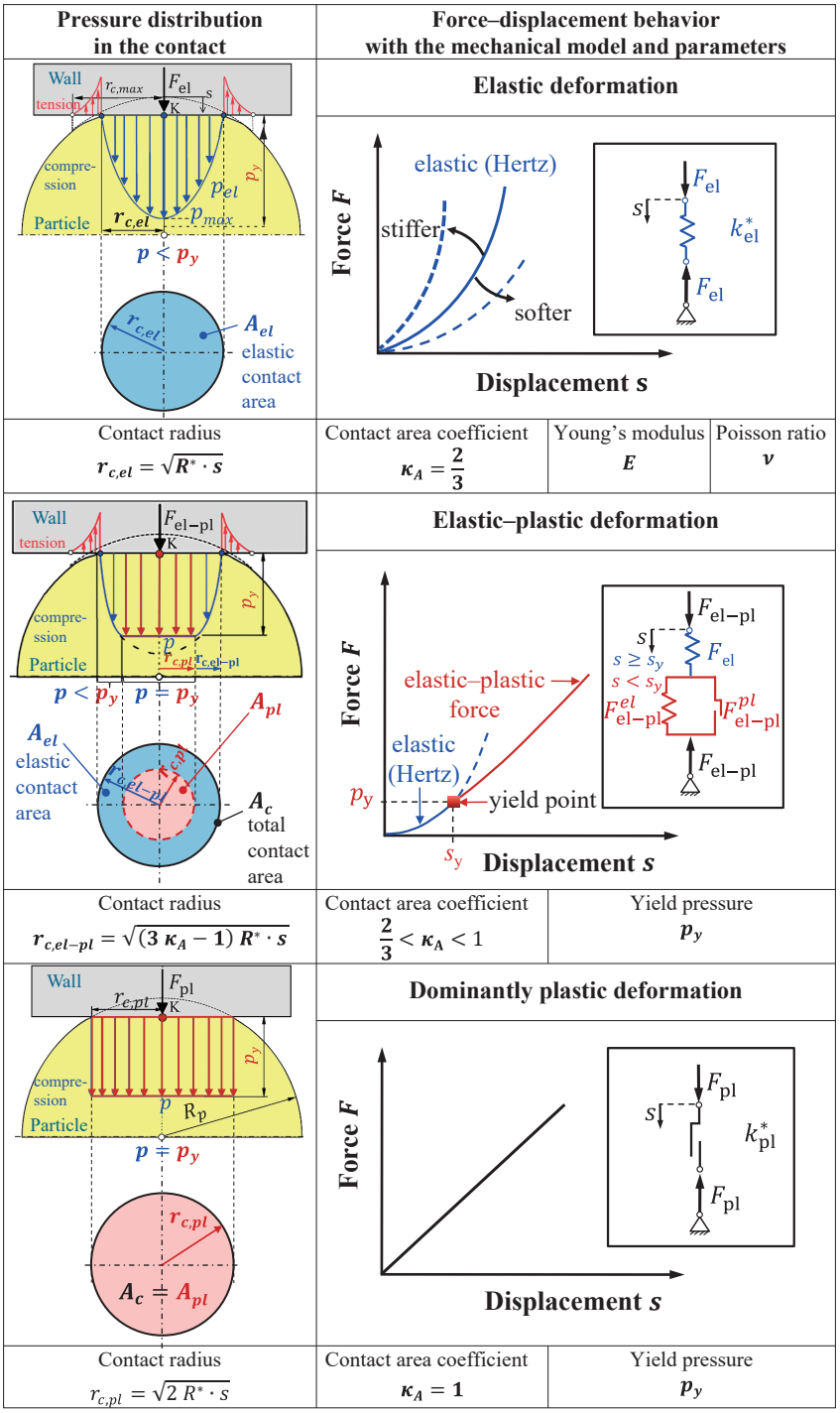

Fig. 3 Characteristic contact pressure distributions and force–displacement relationships for different deformation behavior.

2.2.2 The elastic–plastic part of the force–deformation relationship

The plastic deformation begins when the yield pressure p_y of the material in contact is reached. The force and displacement (F_y, s_y) corresponding to the yield point can be calculated according to Thornton and Ning (1998) as follows:

$$F_y = \frac{\pi^3}{6}\frac{p_y^3}{E^{*2}}R^{*2} \tag{9}$$

$$s_y = \frac{\pi^2}{4}\frac{p_y^2}{E^{*2}}R^{*} \tag{10}$$

These relationships show that the finer particles reach the yield point with lower forces and deformations than the larger particles of the same material, as confirmed by experiments (Antonyuk et al., 2010). Yielding starts at the center of the contact area, at which the yield point is reached due to the highest pressure. With further loading, a plastically deformed circular area A_{pl} of radius $r_{c,pl}$ (**Fig. 3**)

is formed, growing radially from the center outwards to the edge of the full contact area A_c. The outer ring of the contact with the area A_{el} continues to deform elastically because the contact pressure is below the yield pressure. Tomas (2007a) defined an elastic–plastic contact area coefficient κ_A, which describes the ratio of the plastic contact deformation area A_{pl} to the total contact deformation area $A_c = A_{el} + A_{pl}$, as follows:

$$\kappa_A = \frac{2}{3} + \frac{1}{3}\frac{A_{pl}}{A_c} = \frac{2}{3} + \frac{1}{3}\left(\frac{r_{c,pl}}{r_c}\right)^2 = 1 - \frac{1}{3}\sqrt[3]{\frac{s_y}{s}} \tag{11}$$

The ratio A_{pl}/A_c is 0 for ideal elastic ($A_{pl} = 0$) and 1 for fully plastic deformation ($A_{el} = 0$). Therefore, the contact area coefficient κ_A is in the range between 2/3 for ideal elastic behavior and 1 for fully plastic contact deformation. This parameter can also be determined in **Eqn. (11)** as the ratio of the yield point displacement s_y to the total displacement s.

The contact force during elastic–plastic deformation can be determined by integrating the pressure distribution over the corresponding elastic and plastic partial surface areas:

$$\begin{aligned} F_{el-pl} &= \underbrace{\left(\int_0^{r_{c,pl}} p_y \cdot 2\,\pi\, r_c\, \mathrm{d}r_c\right)}_{\text{plastic}} + \underbrace{\left(\int_{r_{c,pl}}^{r_{c,el-pl}} p_{el} \cdot 2\,\pi\, r_c \mathrm{d}r_c\right)}_{\text{elastic}} \\ &= \left[\underbrace{(2-2\kappa_A)}_{\text{elastic}} + \underbrace{(3\kappa_A - 2)}_{\text{plastic}}\right] \cdot \underbrace{(3\kappa_A - 1) \cdot \pi\, R^* \cdot s}_{\text{contact area } A_c} \cdot p_y \end{aligned} \tag{12}$$

For materials with low yield strength, elastic deformation can be neglected, and the contact behavior can be characterized as dominantly plastic with a constant pressure p_y over the whole plastically deformed contact area ($A_c = A_{pl}$, $\kappa_A = 1$) (**Fig. 3**). In this case, the plastic force F_{pl} can simply be derived from **Eqn. (13)** as follows:

$$F_{pl} = \underbrace{2\,\pi\, R^* \cdot s}_{\text{contact area } A_c} \cdot p_y \tag{13}$$

The linear force–displacement relationship for perfectly plastic deformation results in a constant stiffness, given as

$$k_{pl} = \frac{\mathrm{d}F_{pl}}{\mathrm{d}s} = 2\,\pi\, R^* \cdot p_y \tag{14}$$

For the description of the force during elastic–plastic and plastic deformation with this model, only one parameter is needed: the yield pressure p_y, which can be estimated from the yield point in measured force–displacement curves using **Eqns. (9)** and **(10)**.

2.2.3 The loading–unloading behavior

The loading–unloading cycle of an elastic–plastic particle is shown schematically in **Fig. 4**. The unloading process starts at point U (F_{max}, s_{max}) and ends when the force decreases to zero at point E. The force–displacement relationship $F_{un}(s)$ for the unloading phase (curve UE in **Fig. 4**) can be described (Hesse et al., 2023) as

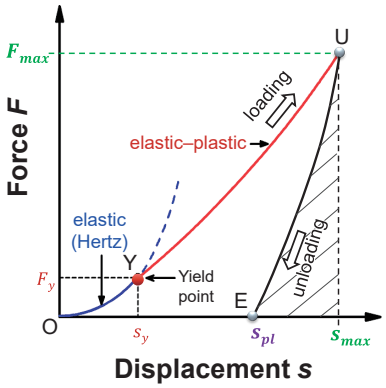

Fig. 4 Schematic representation of the loading–unloading cycle for the elastic–plastic contact.

$$F_{un} = F_{max}\sqrt{\left(\frac{s - s_{pl}}{s_{max} - s_{pl}}\right)^3} \tag{15}$$

During unloading, the elastic part of the deformation is restored. To describe the remaining plastic deformation s_{pl} and the corresponding contact area $A_{pl}(s_{pl})$, the energy conservation law can be applied, which states that the elastic energy stored during the loading phase $E_{el,lo}$ is completely released during the unloading phase $E_{el,un}$. These energies can be determined by integrating the corresponding force–displacement relationships.

The elastic energy of the loading can be calculated as the sum of the total energy before the yield point and the elastic part of the energy during elastic–plastic deformation:

$$\begin{aligned} E_{el,lo} &= \int_0^{s_y} F_{el}\, \mathrm{d}s + \int_{s_y}^{s_{max}} F_{el-pl}^{el}\, \mathrm{d}s = \left[\frac{8}{15} E^* \cdot s_y \sqrt{R^* \cdot s_y^3}\right] \\ &+ \left[\frac{\pi}{10}\, p_y \cdot R^* \left(-\sqrt[3]{s_y s_{max}^5}\left(5\sqrt[3]{\frac{s_y}{s_{max}}} - 8\right) - 3\, s_y^2\right)\right] \end{aligned} \tag{16}$$

The elastic energy released during unloading can be determined as

$$E_{un} = \int_{s_{pl}}^{s_{max}} F_{un}\, \mathrm{d}s = \frac{2}{5} F_{max}(s_{max} - s_{pl}) \tag{17}$$

The plastic deformation can be derived by **Eqn. (18)**

$$\begin{aligned} s_{pl} &= s_{max} - \frac{F_y\, s_y}{F_{max}} \\ &+ \frac{\frac{1}{4}\pi\, p_y \cdot R^* \left(s_{max}^2 \sqrt[3]{\frac{s_y}{s_{max}}}\left(5\sqrt[3]{\frac{s_y}{s_{max}}} - 8\right) + 3 s_y^2\right)}{F_{max}} \end{aligned} \tag{18}$$

2.3 Contact model parameters and measurement methods

The contact behavior of particles is described by contact models using various parameters and properties that can be divided into three main categories (**Fig. 5**):

- Single particle properties, e.g., size, shape, density, and porosity, roughness, modulus of elasticity, stiffness, yield pressure, and surface energy
- Contact interactions, e.g., coefficients of restitution, sliding and rolling friction coefficients, and the Hamaker constant
- Bulk material behavior, e.g., packing density, compressibility, discharge velocity, repose and slope angles, friction coefficient, Hamaker constant

The measurement methods for the first two groups of properties are important for estimating the contact model parameters, which are based on the equivalent properties of both contact partners. Parameters, such as the equivalent modulus of elasticity in **Eqn. (5)**, can be calculated from the properties measured using the first group of methods. However, because of the lack of generalized models for equivalent parameters of the second group, such as the coefficient of restitution, a measurement with both contact partners is always necessary for their determination.

The bulk tests of the third group of methods, shown in **Fig. 5**, are used to validate contact models and calibrate parameters while considering the complexity of particle loading in multiple contacts within a particle system (Coetzee and Scheffler, 2023; Forgber et al., 2022; Grohn et al., 2022b; Handl et al., 2017; Hoshishima et al., 2021; Pachón-Morales et al., 2019; Slominski et al., 2007).

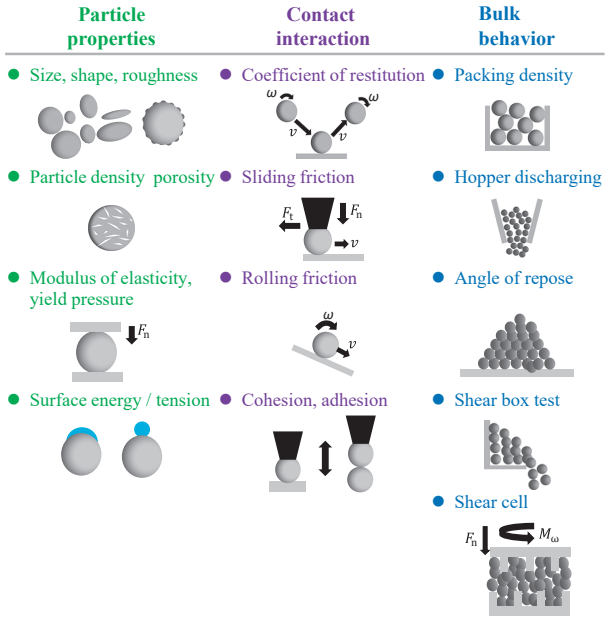

Fig. 5 Schematic overview of contact model parameters and single and bulk measuring methods.

2.3.1 Single particle properties

The particle size and shape distributions are essential dispersity parameters of granular systems (Lu et al., 2015). Detailed knowledge of the dispersity of particulate systems is a key factor in describing their behavior in technological processes.

The established methods for measuring particle size distributions (PSD) in gas and liquid include static and dynamic light scattering, sedimentation in analytical centrifuges, focused beam reflectance measurements, and ultrasonic and light spectroscopic extinction (Merkus, 2009; Schwarz et al., 2018; Tsotsas and Mujumdar, 2011). These methods describe the PSD of granular media using equivalent-diameter approaches in a size range depending on the measurement method. With imaging methods like dynamic image analysis and scanning electron microscopy, the shape of the particles can be described in 2D to provide additional information. For measuring 3D particle shape, computed tomography has become an increasingly common technique (Bagheri et al., 2015; Ditscherlein et al., 2020; Zhao and Wang, 2016). The shape and microstructure of the particles and agglomerates can be reconstructed from the resulting image stack (Dosta et al., 2016) and implemented in the DEM using the multi-sphere or bonded particle approaches (**Fig. 6**). The further benefit of computed tomography is the determination of the porosity of particles and agglomerates, which influences their breakage behavior during loading (Dosta et al., 2016; Lv et al., 2021).

Pores in particles can be divided into open and closed pores, which can be determined using different methods. The closed pores can be calculated by comparing the true density of the material with the results of a gas pycnometer measurement (Amoozegar et al., 2023; Sereno et al., 2007). Gas adsorption methods permit the analysis of open micro- and mesopores with a size range of approximately 0.35–100 nm by adsorption curves using the BJH (Barrett et al., 1951) or HK (Horváth and Kawazoe, 1983) approaches. The investigation of open pores up to 500 µm can be investigated using mercury intrusion porosimetry (Ge et al., 2023; Palmer and Rowe, 1974).

The surface roughness of the particle and wall surfaces is of significance, given their effect on friction (Fuchs et al., 2014; Han et al., 2018; Sheng et al., 2016), reduction of

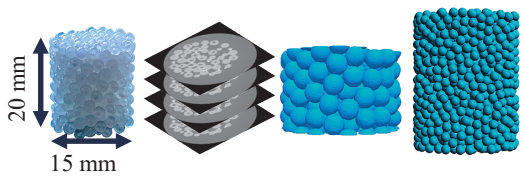

Fig. 6 Implementation of a real agglomerate in the DEM using µCT (TomoScope L, Werth Messtechnik GmbH). From **Left** to **right**: Optical image, image stack from µCT, STL 3D reconstruction, DEM simulation.

cohesion and adhesion (Rabinovich et al., 2000; Rumpf, 2012; Schaefer et al., 1995; Zhou et al., 2003), and collision behavior for dry and wet particle systems (Joseph et al., 2001; Krull et al., 2021; Li et al., 2020a). The roughness of particles can be measured using scanning probe microscopy (SPM), such as atomic force microscopy (AFM) (Ramakrishna et al., 2011) or triboindentation (Krull et al., 2021). The probe is in contact with the surface by applying a defined normal force F (**Fig. 7**). By moving horizontally, the distance of the probe was adjusted to keep the applied normal force constant. The measurement of height variation provides a description of surface topography.

The resolution of the SPM depends on the geometry of the tip and is reduced as the size of the tip decreases. Due to direct contact with the sample, excessive force may have an adverse effect on the surface topography. Therefore, noncontact methods, such as confocal microscopy (Ji et al., 2021) , are preferred, but these are limited to highly curved surfaces.

To calculate the roughness (nm scale), the particle curvature (µm up to mm scale) was separated from the measured surface, as shown in **Fig. 8**.

The mechanical properties of individual particles, such as Young's modulus, yield, and compression strength, can be obtained via uniaxial compression and indentation tests (Antonyuk et al., 2010; Hesse et al., 2020). The load and displacement ranges that can be applied in these tests depend on the size and deformation behavior of the particles. The AFM can be used to measure forces in the range of pN to µN. This method is limited by the particle size, which should be less than 100 µm (Butt et al., 2005; Götzinger and Peukert, 2003; Hodges et al., 2002). For larger and stiffer particles, a nanoindenter (from nN to N) (Fischer-Cripps and Nicholson, 2004) or a material testing machine (from mN to kN and above) can be used.

Fig. 7 Sketch of scanning probe method (SPM).

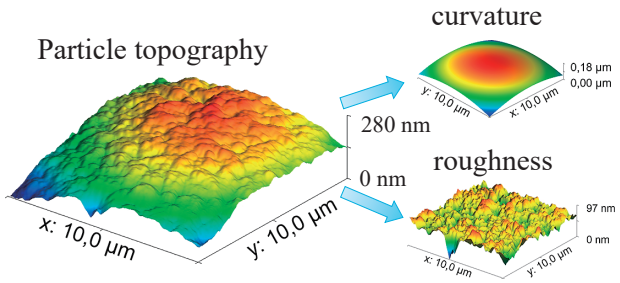

Fig. 8 Measuring topography of a spherical 300 µm zirconium oxide particles using SPM with a triboindenter (TI Premier). The surface roughness was obtained by subtracting the particle curvature.

Fig. 9 shows a typical force–displacement curve for α-lactose monohydrate particles (FlowLac90 from Meggle AG) measured using a Hysitron TI Premier nanoindenter with a circular diamond flat punch (diameter of 100 µm). The particles were nearly spherical in the size range of 200–250 µm.

At the beginning of the contact between the indenter and the particle, elastic deformation of the particle occurs. The force during elastic deformation was described by the Hertz theory in **Fig. 9 (left)**. The value of the modulus of elasticity $E = 2.50 \pm 0.80$ GPa, calculated with **Eqn. (7)** by assuming a Poisson's ratio of $\nu_p = 0.2$, agrees well with measurements for α-lactose in the literature (Perkins et al., 2007).

At the yield point (F_y, s_y) in **Fig. 9**, plastic deformation begins, as indicated by the increasing deviation of the experimental curve from the Hertz curve. The yield pressure $p_y = 27.0 \pm 0.53$ MPa was calculated using **Eqns. (9)** and **(10)** from the obtained displacement and force at the yield point. With these parameters, the force in the elastic–plastic deformation range was approximated by the elastic–plastic model in **Eqn. (12)**. The small deviation of the theoretical curve from the experimental data can be explained by the fact that the contact area of the particle under compression was not perfectly circular, and the particle surface had significant roughness (**Fig. 9, left**).

The unloading model in **Eqn. (15)** was calculated using only the measured material parameters E and p_y. **Fig. 9** shows that the model accurately describes the unloading force and overestimates the plastic deformation (**Eqn. (18)**), but the difference is less than 12 %.

The adhesion and cohesion of a particle depend on its surface energy (Mader-Arndt et al., 2017). The most widely used method for measuring surface energy is the determination of the contact angle of a droplet deposited on a solid surface (Law and Zhao, 2016; Packham, 2003) using camera recordings (**Fig. 10**). By using at least two different liquids with known surface tension and their polar

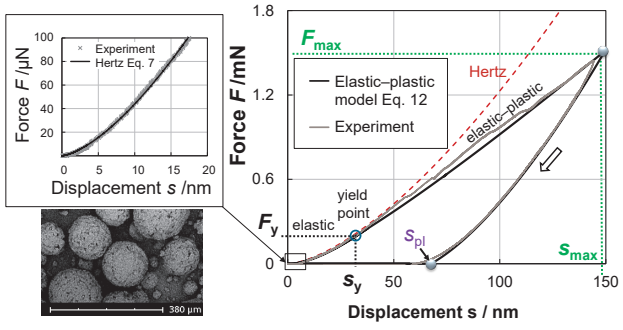

Fig. 9 Typical loading–unloading force–displacement curve during the compression tests of a lactose particle with a flat punch of the nanoindenter device and comparison with the elastic–plastic model (**Section 2.2**), adapted with permission from Ref. (Hesse et al., 2020). Copyright: (2020) Elsevier B.V.

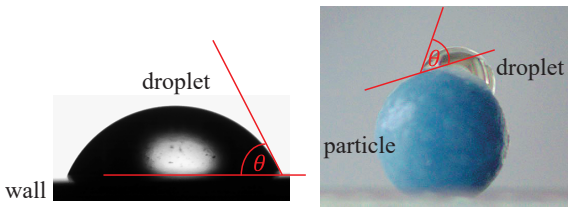

Fig. 10 Contact angle measurements on flat surfaces (**left**) and on particles (**right**).

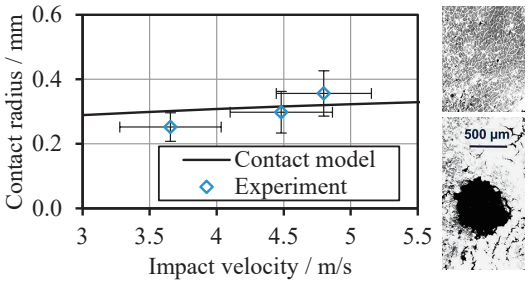

Fig. 11 Comparison of the measured contact radius on a glass substrate coated with Aerosil® R 202 nanoparticles (**right**) with a theoretical value calculated using the plastic contact model (**Fig. 3**), adapted with permission from Ref. (Weis et al., 2019). Copyright: (2019) Elsevier B.V.

and disperse fractions, the surface energy of the material can be determined using the model of Owens, Wendt, Rabel, and Kaelble (Owens and Wendt, 1969).

The surface energy can also be determined using inverse gas chromatography (iGC) (Mohammadi-Jam and Waters, 2014; Rudolph and Hartmann, 2017). Instead of using a liquid phase, polar and unipolar liquids are vaporized and passed through the sample material with an inert gas. By measuring the retention time, the adsorption behavior was investigated, and the surface energy distribution was obtained.

2.3.2 Contact interactions

The various micro processes during particle–particle or particle–wall interactions, such as adhesion (Rabinovich et al., 2000; Tomas, 2007b), friction (Johnson, 1987; Krull et al., 2018; Luding, 2008; Mindlin and Deresiewicz, 1953; Popov, 2017; Sommerfeld and Huber, 1999; Staedler et al., 2019), and plastic deformation (Antonyuk et al., 2010; Molerus, 1975; Paul et al., 2014; Walton and Braun, 1986), can lead to energy dissipation in the contact and significantly influence the behavior of the particle system.

The energy dissipation during a collision is often described by the coefficient of restitution (CoR), e, which is an essential damping parameter in contact models of DEM (Antonyuk et al., 2010; Kruggel-Emden et al., 2007; Luding, 2004; Pöschel and Schwager, 2005; Tsuji et al., 1992). The CoR is defined as the square root of the ratio of the kinetic energies of the particle after ($E_{\mathrm{kin,rebound}}$) and before ($E_{\mathrm{kin,impact}}$) a collision:

$$e = \sqrt{\frac{E_{\mathrm{kin,rebound}}}{E_{\mathrm{kin,impact}}}} = \frac{|v_{\mathrm{R}}|}{|v|} \tag{19}$$

In the case of an ideal elastic impact, the kinetic impact energy is completely stored during the approach of the colliding partners (loading phase) and released during their rebound (unloading phase). Therefore, the relative velocities of the contact partners before (v) and after (v_{R}) the impact are equal and $e = 1$. Conversely, if the energy of the kinetic impact is completely dissipated during the collision, there is no rebound, and $e = 0$. For partial dissipation of the impact energy, e.g., in the case of elastic–plastic deformation behavior, the restitution coefficient is in the range of $0 < e < 1$ (Antonyuk et al., 2010; Johnson and Pollock, 1994; Stronge, 2010; Thornton and Ning, 1998). The CoR depends not only on the deformation behavior of the contact partners but also on the topography of the surfaces (Krull et al., 2018).

To measure CoR, collision experiments between a single particle and a wall and between two particles can be performed as free fall tests (Antonyuk et al., 2010; Bunke et al., 2024; Crüger et al., 2016b; Kharaz et al., 2001; Krull et al., 2018) or pendulum tests (Hlosta et al., 2018; Stevens and Hrenya, 2005; Weir and Tallon, 2005). The velocity of the particles before and after contact is usually obtained by high-speed recording.

The influence of the collision angle and initial particle rotation on the CoR can be studied by tilting the substrate or using a pneumatic setup to accelerate particles at different impact angles (Antonyuk et al., 2010; Dong and Moys, 2006; Kharaz et al., 2001; Krull et al., 2023). Collision tests can be used to determine the coefficient of friction in a sliding regime, which typically occurs at higher impact angles (Kharaz et al., 2001; Maw et al., 1976; Mueller et al., 2011). Moreover, the maximum contact area of the particle can be determined due to the wall coating by nanoparticles with low adhesion (**Fig. 11**) (Weis et al., 2019). During collisions, the coating adheres to the contact surface of the particle, leaving an imprint. The proposed method can be used to evaluate the calculated contact area in the DEM to obtain the actual contact force. The elevated standard deviation observed in the experimental results can be attributed to the non-spherical shape of the particles. Consequently, the noncircular contact area was evaluated using the equivalent radius.

The coefficient of sliding friction between a particle and a wall can be measured by gluing a particle to the cantilever of an AFM (Butt et al., 2005) or on the flat tip of a triboindenter (Fuchs et al., 2014; Strohner and Antonyuk, 2023). The fixed particle (**Fig. 12, left**) is indented into the wall substrate surface with a constant normal force and moved along the surface by measuring the tangential force. For higher loads, the sliding friction can be determined for a monolayer of particles glued to a plate that is sheared along

the wall substrate (**Fig. 12, right**) using a shear cell (Hesse et al., 2020). The coefficient of sliding friction can be calculated according to Coulomb's law of friction (Mullier et al., 1991; Popov, 2017).

Fig. 13 shows the measured friction coefficients for spherical zirconium oxide particles (912 µm in diameter) in contact with an untreated stainless steel substrate using the single particle test with a triboindenter (Ti Premier, Hysitron) and the shear test of the particle monolayer with a ring shear cell (Powder Flow Tester, Brookfield). The measured friction coefficient demonstrates comparable values for various normal forces between 10 and 10,000 mN. An increase in the friction coefficient can be observed at lower normal forces for single particles due to an increased influence of adhesion. The exhibited standard deviation was derived from three repetitions and does not encompass deviations occurring during a single measurement. At higher forces acting on the particle layer, small variations in the particle size can lead to an uneven load distribution, which results in an increased friction coefficient due to partial wear.

The rolling friction coefficient of spherical particles can be measured by rolling an unfixed particle between the indenter tip and substrate under a reduced normal load. The tangential force on the horizontally moving tip or substrate is then measured by a triboindenter (Bilz and de Payrebrune, 2021; Fuchs et al., 2014; Hesse et al., 2020).

The adhesion between two particles or a single particle and a wall can be measured with the same setup as for sliding friction using an AFM (Butt et al., 2005) or nanoindenter (Mader-Arndt et al., 2017). The adhesion was measured by the indentation of the glued particle in the contact partner. The resulting pull-off force at detachment can be used to calibrate the Hamaker constant in contact models.

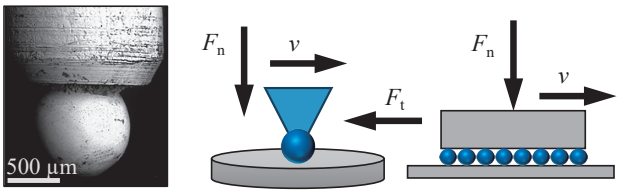

Fig. 12 **Left**: A zirconia particle glued on a flat indenter tip for a triboindenter, adapted with permission from Ref. (Strohner and Antonyuk, 2023). Copyright: (2023) Elsevier B.V. **Middle/right**: Schematic of the sliding friction measurement method for single particles and particle monolayers.

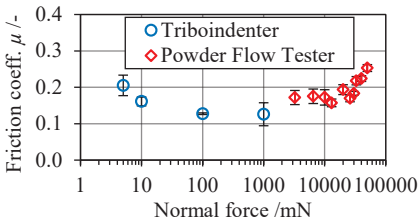

Fig. 13 Measured sliding friction coefficients of zirconium oxide particles in a stainless steel wall via single-particle triboindentation and monolayer shear test.

2.3.3 Bulk parameter adjustment methods

Due to the variety of particle properties in a granular system, a more complex stress state in multiple contacts, and overlapping effects, the coefficients of friction and the cohesion measured in bulk tests can deviate from single-particle measurements (Härtl and Ooi, 2011; Jones, 2003). Therefore, the contact model parameters obtained from single particle tests must be adjusted using bulk test methods, which always reflect the superposition of friction and cohesion/adhesion forces in multiple contacts. However, single particle measurements are of great importance for obtaining the real contact behavior of particles for the selection or development of a suitable contact model.

The simplest experiment for the validation and calibration of the bulk behavior was to measure the packing density of the granular media. By filling a defined cylindrical container with the particle sample with a known mass, the height can be measured and compared with the DEM simulation results (Gao et al., 2021; Hesse et al., 2021). By vibrating this container, the tapped density, which characterizes the compaction behavior of the material due to the change in the spatial arrangement of particles during vibration, can also be measured and compared with the DEM (Abi-Mansour et al., 2018).

A common method to investigate bulk behavior with a free surface is the measurement of the angle of repose (AoR). The AoR can be measured in both static (Nakashima et al., 2011; Quist and Evertsson, 2015; Roessler and Katterfeld, 2019) and dynamic (Cunha et al., 2016; Santos et al., 2016) cases (**Fig. 14**). In the static case, a cylinder on a plate is first filled with the bulk material and then slowly lifted (Grima and Wypych, 2011; Hesse et al., 2021). The slope of the resulting pile was measured. Using a rotating drum, the dynamic AoR can be measured (Coetzee, 2019). By varying the rotational speed, the particle behavior can be investigated for a wider range of forces acting on the particles.

Ring and translational shear cells can be used to obtain bulk coefficients of friction and cohesion and validate flow behavior during silo discharge (Angus et al., 2020; Hesse et al., 2020; Tykhoniuk et al., 2007). The simulations of the flow behavior at low stresses can be validated using a powder rheometer. For this test, a cylindrical cell with a stirrer (**Fig. 15**) was integrated into a rotational rheometer to measure the resulting torque during the stirrer rotation inside the bulk material (Hesse et al., 2020). By varying the stirrer depth in the cell, the flow behavior under different normal stresses can be studied.

Hopper discharge or draw-down tests (Coetzee, 2020; Ketterhagen and Wassgren, 2022) with small transparent

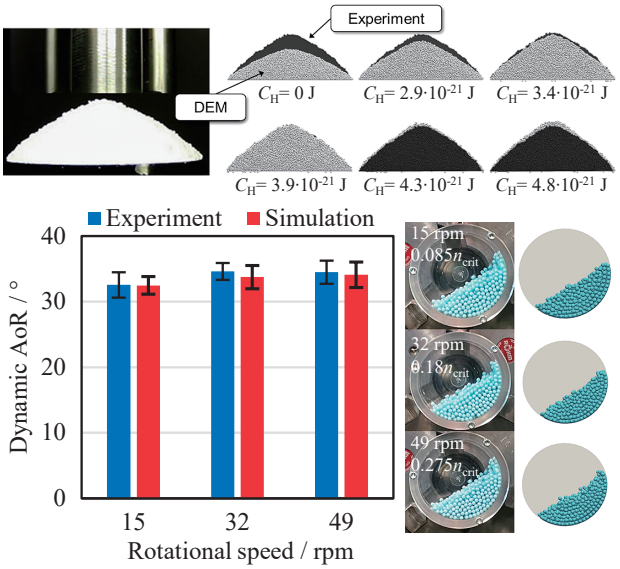

Fig. 14 **Top**: Adjustment of the Hamaker constant of 200 µm lactose particles, adapted with permission from Ref. (Hesse et al., 2020). Copyright: (2020) Elsevier B.V. **Bottom**: Dynamic AoR of the coated zirconia particles (3 mm). In both cases, the Hertz–Mindlin model was used. A cohesion model based on Hamaker was implemented for lactose particles.

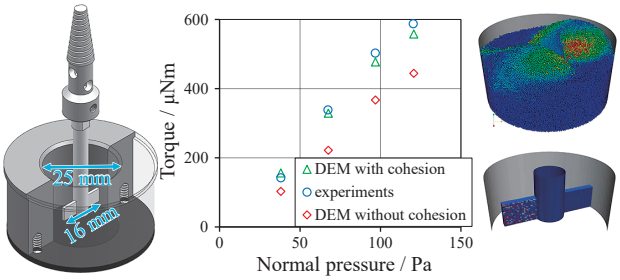

Fig. 15 Powder rheometer setup and comparison of the measured torque with the DEM simulation of lactose particles using the Hertz–Mindlin model and adjusted cohesion parameter, adapted with permission from Ref. (Hesse et al., 2020). Copyright: (2020) Elsevier B.V.

wedge-shaped and conical hoppers can be performed by comparing the flow inside the hopper with the discharge mass flow. In the case of the wedge geometry, the outlet angle of the hopper can be varied to change the flow behavior and validate the simulation results. A disadvantage of this method is the large number of particles required for the DEM simulation. A combined investigation of the flow behavior and AoR can be performed using a shear box test (Carr et al., 2023; Hesse et al., 2021; Roessler et al., 2019). The test comprised a cubic box with transparent walls, including a horizontal removable wall. The particles were introduced into the box, and the static AoR inside the box was measured. After removing the horizontal wall, the mass flow was measured by a high-speed balance.

3. Contacts in two- and three-phase systems

Liquids in particle processes can significantly influence particle behavior and contact dynamics. This can be considered in DEM simulations using different approaches. A popular approach is coupling with computational fluid dynamics (CFD), which simulates the behavior of the fluid phase and transfers fluid forces on particles to the DEM (Di Maio and Di Renzo, 2007; Tsuji, 1993). The fluid–particle interactions can either be resolved in the simulation (Tang et al., 2017b) or calculated by applying a drag model (Li et al., 2016). Due to the significant increase in the computational cost of the resolved simulations, unresolved CFD-DEM simulations are preferred. In this case, the influence of the liquid on the contact dynamics should be considered. In addition, the influence of the particle concentration (swarm effect) must be taken into account by specific correlations for the drag forces (Deen et al., 2007; Deshpande et al., 2019, 2020; Golshan et al., 2020).

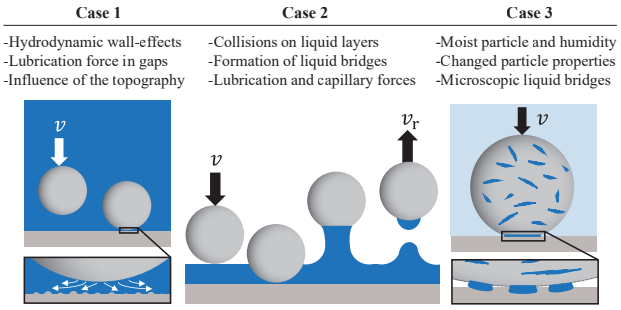

Fig. 16 Schematic of liquid effects on particle collisions.

3.1 Contact modeling based on liquid

The liquid effects on the particle contact can be calculated directly in the DEM simulation with modified contact models. In the following sections, different approaches to modeling wet contact are explained for specific contact scenarios. The modeled influences can be divided into three main cases (**Fig. 16**). The first case considers the influence of hydrodynamic effects on the gap between approaching and rebounding contact particles or between a particle and wall. These effects typically occur when particles collide in a liquid environment, such as a suspension or paste. The second case describes the formation and rupture of liquid bridges in contact. This is a typical example of the impact of liquid-layer particles on surfaces. During particle rebound, liquid bridges are formed, leading to capillary forces. Another effect in the third case was the moisture saturation of the porous particles and the humidity of the surrounding gas.

3.1.1 Near-wall effects

The influence of liquid forces on contact behavior can be considered by modifying the parameters of contact models without adding new force terms (Jain et al., 2012). An example of a parameter that can be affected by the surrounding medium is the friction coefficient. Sinka (2007)

reported a significant decrease in friction due to lubrication effects during powder compaction in a die. According to the work of Kuwagi et al. (2000), the shear force in a wet contact can be expressed as the internal friction in liquid. The viscous energy dissipation due to fluid displacement at the contact can be considered in the DEM by modifying the restitution coefficient. A well-known approach to this is an elastohydrodynamic model (Barnocky and Davis, 1988), which describes the wet coefficient of restitution, e_{wet}, as

$$e_{wet} = e_{dry} + \frac{1+e_{dry}}{St} \ln \frac{h_{init}}{h_{min}} \tag{20}$$

depending on the Stokes number St:

$$St = \frac{m_P \cdot v}{6\pi \cdot \eta_f \cdot R_p^2} \tag{21}$$

where η_f is the dynamic viscosity, h_{init} is the initial distance between particles, below which the viscous squeezing flow begins, and h_{min} is the critical distance at which this flow is interrupted by surface roughness (Joseph et al., 2001; Krull et al., 2021).

The energy dissipation of the wet collision can lead to sticking, which can be estimated using the critical Stokes number. The Stokes criterion according to Ennis et al. (1991) takes into account the energy dissipation due to viscous effects in the liquid layers on the colliding particles, assuming that no plastic deformation occurs, but some of the kinetic impact energy can be dissipated due to inelastic contact deformation. If the critical Stokes number defined as $St^* = \left(1+\frac{1}{e}\right)\ln\left(\frac{h_{init}}{h_{min}}\right)$ (Barnocky and Davis, 1988) is exceeded, the particle is expected to rebound. Liu et al. (2000) extended this criterion to plastic contact deformation.

The wet coefficient of restitution can be applied in DEM simulations as a parameter to model particle contact while considering hydrodynamic effects (Sutkar et al., 2015).

As an alternative to the elastohydrodynamic model, the lubrication forces can be implemented directly into the force balance of the DEM and calculated in each wet contact at small particle distances (Grohn et al., 2022b; Nijssen et al., 2023).

The lubrication force $F_{L,n}$ in normal direction (Grohn et al., 2023a; Lian et al., 1998; Shi and McCarthy, 2008; Tang et al., 2017a) is usually described in DEM by the Adams and Perchard (1985) model in **Eqn. (22)** based on the Reynolds lubrication theory. For thin liquid layers, the expression of Matthewson (1988) can be used. For the lubrication force in tangential direction $F_{L,t}$ different models were developed (Goldman et al., 1967; Kuwagi et al., 2000; Washino et al., 2017). The analytical solution of Popov (2017) in **Eqn. (23)** was derived for the tangential force on a spherical particle moving along a flat surface covered by a liquid film.

$$F_{L,n} = \frac{6\pi \cdot \eta_f \cdot R^{*2} \cdot v_n}{h} \tag{22}$$

$$F_{L,t} = 2\pi \cdot \eta_f \cdot R^* \cdot v_t \cdot \ln\left(1+\frac{R^*}{2h}\right) \tag{23}$$

where v_n and v_t are the normal and tangential components of the relative velocity of the colliding particles, respectively, and h is the shortest distance between their surfaces. In direct contact, h would become zero, resulting in an infinite force. In general, two options are used to exclude this event. The first method is to define a cut-off distance h_{min}, which sets a limit on the minimum applied value of h. The second method uses an extended distance s_r which is added to h as

$$F_{L,n} = \frac{6\pi \cdot \eta_f \cdot R^{*2} \cdot v_n}{h + s_r} \tag{24}$$

The parameters h_{min} and s_r refer to the physical presence of the surface asperities that first come into contact during the collision. Therefore, they can be derived from measurable roughness parameters, such as the root mean square roughness (Krull et al., 2021; Mongruel and Gondret, 2020; Strohner and Antonyuk, 2023).

3.1.2 Liquid bridge modeling

In many particulate three-phase processes, such as fluidized bed agglomeration, rotary drum coating, and mixing, the presence of a liquid phase in the form of films on solid particles or droplets can significantly affect particle dynamics due to the formation of liquid bridges. The capillary forces acting in liquid bridges between particles due to interfacial surface tension can lead to particle sticking and aggregation. To describe these effects, the contact forces in DEM are usually extended by a liquid bridge model (Endres et al., 2021; Wu et al., 2018).

The capillary force in the liquid bridge can be derived from the Young–Laplace equation by applying a shape model of the liquid bridge. Many models have been developed to describe capillary forces in symmetrical liquid bridges under static and dynamic conditions (Megias-Alguacil and Gauckler, 2009; Mikami et al., 1998; Pitois et al., 2001; Xiao et al., 2020). The liquid bridge model of Israelachvili (2011) distinguished the capillary forces in the liquid bridge between two particles and the particle on the flat wall as

$$F_{cap,pp} = \frac{-4\pi R^* \cdot \gamma \cdot \cos\theta}{1+\left(\sqrt{1+\frac{V_b}{\pi R^* \cdot h^2}}-1\right)^{-1}} \tag{25}$$

$$F_{cap,pw} = \frac{-8\pi R^* \cdot \gamma \cdot \cos\theta}{1+\left(\sqrt{1+\frac{V_b}{\pi R^* \cdot h^2}}-1\right)^{-1}} \tag{26}$$

where γ denotes the surface tension and θ is the wetting angle. The volume of the liquid bridge V_b formed during the rebound of wetted particles can be determined using a liquid transfer model developed by Shi and McCarthy (2008), which defines the distribution and transfer of liquid on the interacting particles.

The maximum liquid bridge length determines the critical distance at which the bridge ruptures, thus limiting the scope of the liquid bridge model. There are several models for the maximum liquid bridge length (Antonyuk et al., 2009; Gollwitzer et al., 2012; Lian et al., 1993; Mikami et al., 1998; Pitois et al., 2001); however, Grohn et al. (2022a) recently showed that the impact velocity, which was not considered in earlier models, significantly affects this parameter. They extended a common model (Mikami et al., 1998) to include the collision velocity. This resulted in the distinct equations for the particle–particle (pp) and the particle–wall (pw) collisions, with C_{pp} and C_{pw} as fluid-dependent constant parameters:

$$l_{max,pp} = (0.99 + 0.62\theta) V_b{}^{0.34} \left(1 + C_{pp} v_{im}\right)^{\frac{2}{3}} \quad (27)$$

$$l_{max,pw} = (0.95 + 0.22\theta) V_b{}^{0.32} \left(1 + C_{pw} v_{im}\right)^{\frac{2}{3}} \quad (28)$$

3.1.3 Moist particle modeling

The moisture content of particles and agglomerates can significantly influence their mechanical deformation and breakage behavior (Iveson et al., 2001; Reynolds et al., 2005). The amount of liquid in the porous material is described by the degree of void saturation S, which is defined as the ratio of the volume of the void occupied by the liquid to the total volume of the void.

Schubert (1984) found that the tensile strength of wet agglomerates strongly depends on their hydro-textural state and divided the saturation degree into three ranges according to the binding mechanisms of the particles by the liquid. At low moisture content, liquid bridges are formed between individual particles and liquid films on their surface. In the so-called pendular region, the capillary forces in the liquid bridges determine the tensile strength $\sigma_{t,ct}$. As the saturation increases ($S > 0.3$), some pores are filled with liquid, leading to the coexistence of liquid bridges and capillary adhesion. Pure capillary adhesion is reached at $S \geq 0.8$. The moist agglomerates showed the highest strength near full saturation, $S \approx 0.9$. The tensile strength in this region can be described by the Schubert model (Schubert, 1984). For the transition region (funicular range), the attractive force cannot be given analytically because of the complexity and diversity of the funicular clusters. Herminghaus et al. (2019) performed simulations for different funicular clusters.

The above works assume quasi-static loading and only consider the dominant capillary forces. However, the deformation and breakage behaviors of moist particles under dynamic loading are strongly influenced by the viscous effects in the liquid distributed in the porous structure. The viscous energy dissipation typically becomes dominant at high loading rates and can be significant by high-viscosity binders (Antonyuk et al., 2009; Crüger et al., 2016a; Davis et al., 2002; Pitois et al., 2000; Rossetti et al., 2003). Fu et al. (2004) found that at least 97 % of the impact kinetic energy is dissipated by viscous flow in the liquid bridge formed in the contact area at low impact velocities or by bulk viscoplastic flow at higher impact velocities.

Tardos et al. (1997) showed that the strength of wet viscoplastic pellets depends on the viscous forces and can be described by the Stokes deformation number, which is the ratio of the initial kinetic energy to the deformation energy. Iveson et al. (2002) related the strength of the wet pellets to the capillary number Ca, which describes the ratio of the viscous force to the surface tension force. An important finding from their compression experiments of wet pellets with different Ca contents was that for $Ca > 10^{-4}$ the viscous forces became dominant and significantly influenced the yield strength of the wet particles. In this range of Ca numbers, the adhesion criteria based on the Stokes number (**Eqn. (21)**) and the wet restitution coefficient (**Eqn. (20)**) are used.

Grohn et al. (2020) reported that the stiffness and breakage force of microcrystalline cellulose pellets decreased with increasing saturation. Therefore, saturation-dependent mechanical properties, such as the reduced Young's modulus and yield pressure, must be considered (Weis et al., 2019). In addition, energy dissipation during collisions due to the presence of liquid in the particles must be considered. Similar to liquid bridge modeling, capillary and viscous forces can be applied to the contact model. Weis et al. (2021) implemented a liquid force term that acts during particle loading because of the fluid being squeezed out of the particle. During unloading, it was assumed that a liquid bridge with the same volume as the amount of liquid squeezed out would form and act as a capillary force. The applied models are similar to the described lubrication and liquid bridge models with a modification to account for the geometry change due to deformation in the contact.

Moist air can also have direct effects on particle rebound behavior, as demonstrated by different authors (Dong et al., 2018; Li et al., 2020b), who conducted experiments with µm sized particles at various humidity levels and detected a decrease in the coefficient of restitution with increasing humidity. This was explained by the adhesion resulting from the formation of microscopic liquid bridges during contact.

3.2 Determination of fluid properties

Based on the presented models for the consideration of liquids in the contact modeling in DEM, the material

parameters of the involved fluid need to be specified. Usually, the fluid is already known; therefore, the density, viscosity, and surface tension can be found in the literature or might be provided by the manufacturer. Otherwise, e.g., if a fluid mixture with unknown properties is investigated, these properties need to be measured. The density can be determined by gravimetric analysis. Various methods exist for the viscosity measurement; therefore, the selection of a suitable method will depend on the investigated fluid as well as the available options, e.g., a draining vessel-type, a falling ball, or a rotational viscosimeter. Bhattad (2023) presents an overview of the methods used for viscosity measurements.

The surface tension of a liquid can be determined using different types of tensiometers based on various correlations. They are either based on a force balance or correlate the shape of a droplet or bubble with the applied pressure to determine the surface tension. Franses et al. (1996) summarized different methods for surface-tension measurement.

The contact angle is connected to the surface tension and characterizes the wettability of surfaces by a fluid. A common contact angle measurement method is the analysis of the shape of a single sessile droplet placed on a solid surface. The static contact angle is then optically determined as the angle between the droplet surface contour and the baseline of the surface at the three-phase contact point (**Fig. 10**).

If the three-phase contact line is exposed to highly dynamic influences, the apparent (macroscopic) contact angle may vary from the microscopic contact angle. To account for this effect, a dynamic contact angle can be used, which can be divided into an advancing θ_a and a receding contact angle θ_r. The dynamic contact angle can be measured under the action of forces on the contact line (Butt et al., 2022). Further explanation of the contact angle measurement and additional methods are provided by Law and Zhao (2016).

3.3 Study of liquid effects in single particle experiments

To measure liquid effects on particle collision, many methods developed for single particle experiments in air can be adopted. This requires modification of the test setup and consideration of additional parameters. In some cases, completely new setups have to be developed for estimating specific parameters, including the effects of liquids.

3.3.1 Particle collisions in liquid

The wet coefficient of restitution can be determined similarly to the free fall experiments under dry conditions (**Section 2.3.2**) by measuring the impact and rebound velocities of a single particle dropped onto a wall surface in a chamber filled with the investigated liquid (**Fig. 17**). It is essential that the chamber side walls and liquid are transparent to record particle movements with high-speed cameras (Krull et al., 2021). The chamber should be designed in such a way that the wall effects do not influence particle sedimentation and collision. The impact velocity can be varied up to the terminal velocity by adjusting the drop height of the particle. To prevent the adhesion of gas bubbles to the particle surface as they pass through the interface, the particle release should be positioned inside the liquid.

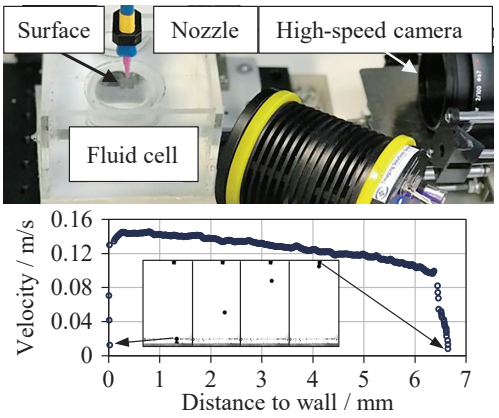

Fig. 17 Experimental setup for investigating particle collisions in liquid (**top**), adapted with permission from Ref. (Krull et al., 2021). Copyright: (2021) Elsevier B.V. Recording of a single 460 µm zirconium oxide particle sediment toward a wall in water with the corresponding velocity profile (**bottom**).

Complementing the wet restitution coefficient, this experiment estimated the hydrodynamic wall effects on particle collision. **Fig. 17** shows the velocity profile of a 460 µm zirconia particle during sedimentation toward a wall in water. After release, the particle is accelerated by gravity. At a distance of around 200 µm from the wall, the velocity of the particle begins to decrease because of the wall effect. The lubrication force exerted a notable influence, particularly in the vicinity of the wall. This wall effect must be considered in the DEM for a correct calculation of the contact force.

A detailed experimental analysis in combination with numerical modeling of particle movement in the vicinity of a wall can also provide information on the influence of surface topography on the lubrication force (Mongruel and Gondret, 2020; Strohner and Antonyuk, 2023). These data can be used to calibrate the asperity height parameter h_{min} in the elastohydrodynamic model (Barnocky and Davis, 1988) in **Eqn. (20)**.

Fig. 18 shows the measured CoR of zirconia particles in the size range of 300–1000 µm colliding in water ($St < 200$) and air ($St > 2000$) with titanium substrates, which differed in their roughness ($S_{RMS,polished} = 33$ nm; $S_{RMS,untreated} = 370$ nm).

For the collisions in air, the higher roughness of the untreated titanium surface resulted in a slight reduction in the mean CoR due to friction effects and plastic deformation of the asperities. However, this was accompanied by an

increase in the standard deviation, which can be attributed to the fact that the surface roughness leads to greater variation in contact scenarios. In the case of collisions in water, a reduction in *St* resulted in a rapid decrease in CoR due to the effect of viscous forces. In contrast to the collision in air, at lower Stokes numbers in water, the rough surfaces exhibit a higher mean CoR than the polished surfaces. This phenomenon can be attributed to the higher minimum gap between the particle and the wall surface asperities, which reduces the effect of viscosity.

In addition to the roughness height, the topographical structure of the surface can also influence the collision behavior. **Fig. 19** shows the measured CoR values of the same zirconia particles for collisions in water and air with titanium substrates with varying surface microstructures. A comparative analysis was conducted between the polished substrate and two additional surface topologies: a truncated pyramidal substrate with a front face of 100 × 100 µm² and an opening angle of 25° and a channel substrate comprising 50 µm grooves and 50 µm bridges, which were produced using micromilling (Aurich et al., 2024). The CoR of the polished substrate decreased with a reduction in *St* and consequently remained nearly constant for the microstructured surfaces during collisions in water (*St* < 200). This can be attributed to the change in fluid dynamics through the microstructure, which results in a decrease in the viscous forces (**Fig. 20**) (Strohner and Antonyuk, 2023). At higher *St* numbers in the absence of liquid influence, the CoR of the microstructured surfaces increased due to the reduced drag exerted on the particles. It remains below that observed for the polished surface, reflecting the increased friction and multiple contacts resulting from particles impacting between two or more structural elements. The variability in contact scenarios on the microstructure also contributes to the high standard deviation of the microstructured surfaces.

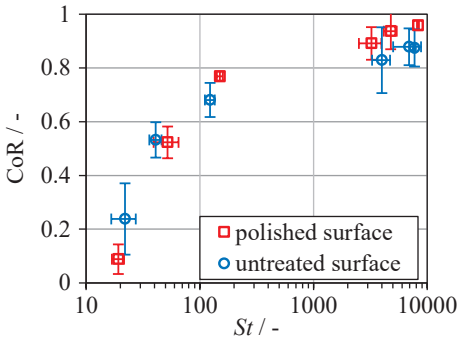

Fig. 18 Comparison of CoR values for zirconium oxide particles in the size range of 300–1000 µm with a polished and untreated titanium substrates in air and water, adapted with permission from Ref. (Krull et al., 2021). Copyright: (2021) Elsevier B.V.

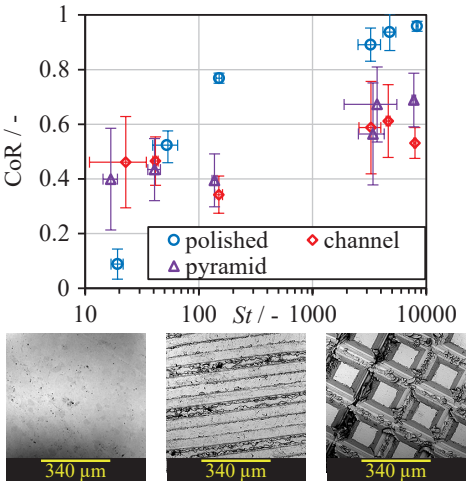

Fig. 19 Comparison of CoR for collision of zirconium particles with titanium substrates in air and water. SEM-images of the substrates are shown below (polished, channel and truncated pyramid).

3.3.2 Particle collision with a wet surface

The influence of the liquid layers covering the particles on their collision and sticking behavior can be considered in the DEM simulation by the wet restitution coefficient e_{wet} as a function of the *St* number as it was described in **Section 3.1.1**. This relationship can be obtained via collision experiments of particles using the setup shown in **Fig. 21**. The particle is dropped onto a substrate covered with liquid. The substrate is placed inside a frame that limits the spreading of liquid and defines the maximum layer height, which corresponds to the distance parameter h_{init} by the calculation of e_{wet} in **Eqn. (20)**.

Since the layer thickness can decrease due to evaporation, Antonyuk et al. (2009) used a precision balance to measure the weight of the layer and calculated the current liquid height by knowing the inner frame area. Crüger et al. (2016b) applied a confocal sensor to measure the current layer thickness. The method demonstrated higher accuracy because the layer thickness was measured locally at the

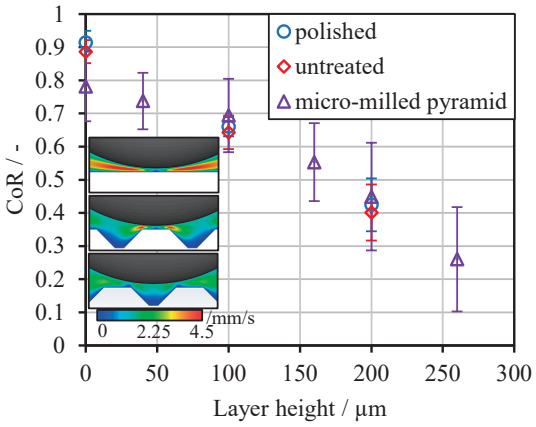

Fig. 20 CoR of zirconia particles on titanium surfaces with different topography covered by water layers of various heights at a collision velocity of 0.5 m/s, adapted with permission from Ref. (Strohner and Antonyuk, 2023). Copyright: (2023) Elsevier B.V.

contact area, thereby avoiding inaccuracies due to tilting of the sample or height variations due to surface curvature.

Fig. 20 shows the CoR measured for zirconia particles (912 µm) colliding on titanium surfaces with different topographies covered by a water layer. While the reduction in CoR with increasing layer height for the polished and untreated surfaces was comparable, the CoR on the micro-milled surface decreased at a slower rate. This result is due to the reduced lubrication force, which is similar to that in the liquid-immersed experiments. The microstructure of the pyramid surface leads to a high standard deviation, as the collision behavior depends on the contact position, which in turn determines the contact geometry.

A key issue in studying wet particle–particle collisions is the creation of a defined liquid layer on the particle surface before contact. Buck et al. (2018) developed a setup, in which the particle is wetted as it passes through a liquid film bounded by a ring. Bunke et al. (2024) extended the experimental procedure of Buck and described the liquid layer height formed on the particle surface after penetration.

3.3.3 Investigation of liquid bridges

The mechanisms of shape change and rupture of the liquid bridge can be studied by high-speed imaging (**Fig. 22**) in free fall collision experiments, as described in the previous section. As illustrated in the models in **Eqns. (27)** and **(28)**, the critical liquid bridge length depends on the collision velocity and differs between particle–particle and particle–wall collisions. The range of adjustable test velocities in the free fall collision setup (**Fig. 21**) was constrained by the particle acceleration due to gravity up to a terminal velocity.

For liquid bridge investigations over an extended range of velocities, two additional setups can be used (Grohn et al., 2022a). The first setup shown in **Fig. 23** performs slow dynamic tests at velocities between 0.1 and 40 mm/s using a material testing machine, e.g., Texture Analyzer (TA). The particle is glued to the punch of the TA, while the fluid is applied as a droplet to the second particle or substrate fixed to the sample table. The droplet volume can be precisely specified using an Eppendorf pipette, which corresponds to the liquid bridge volume. First, the punch moved the fixed particle to the wetted surface. After contact, the particle is separated from the wall surface as the punch moves upward at a defined velocity. The formed liquid bridge is stretched until it ruptures.

Higher velocities can be achieved using the second setup (**Fig. 24**) by moving the attached particle with a pneumatic cylinder. By using different cylinder sizes and varying the applied pressure through a pressure throttle, separation velocities between 0.3 and 4 m/s can be set. The measurement procedure was the same as that for the low-velocity setup.

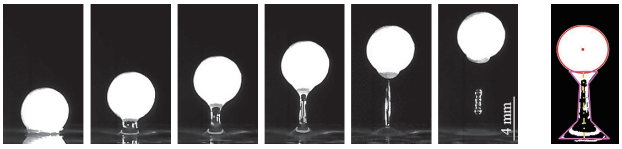

Fig. 22 Formation and rupture of the liquid bridge during particle rebound from the wall covered by a liquid layer with a thickness of 100 µm (**left**) and approximation of the liquid bridge geometry (**right**).

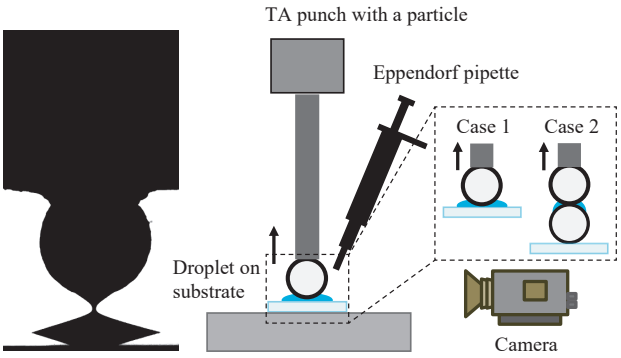

Fig. 23 Schematic of the low-speed liquid bridge experiment (0.1–40 mm/s) using TA, adapted with permission from Ref. (Grohn et al., 2022a). Copyright: (2022) Elsevier B.V.

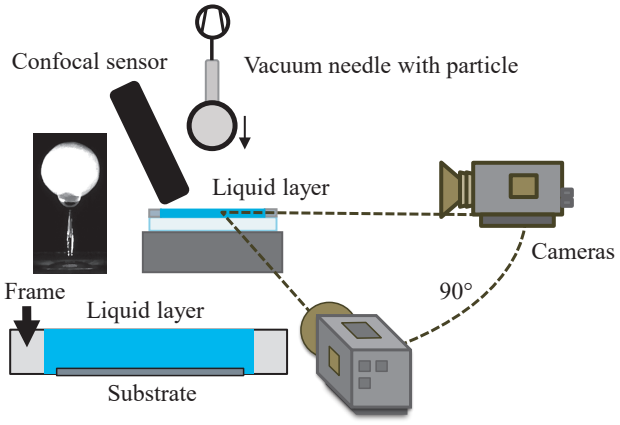

Fig. 21 Schematic of the free fall setup for particle collision on a wall surface covered with a liquid layer, adapted with permission from Ref. (Grohn et al., 2022a). Copyright: (2022) Elsevier B.V.

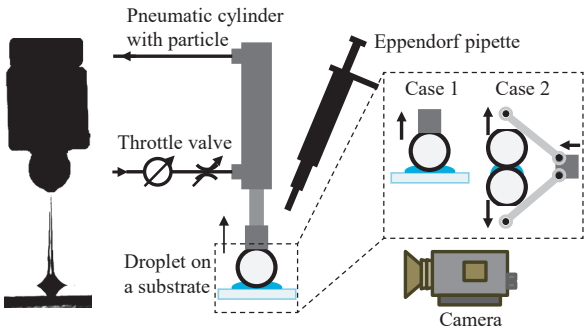

Fig. 24 Schematic of the high-speed liquid bridge experiment (0.3–4 m/s) using a pneumatic cylinder, adapted with permission from Ref. (Grohn et al., 2022a). Copyright: (2022) Elsevier B.V.

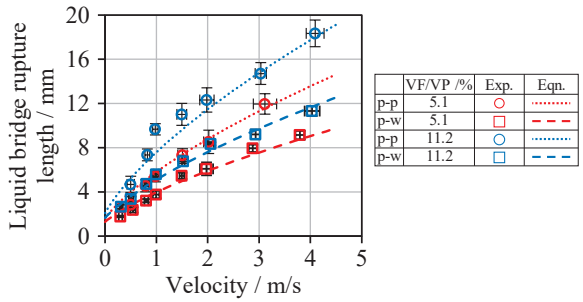

Fig. 25 Influence of impact velocity and liquid/particle volume ratio on maximum liquid bridge length: comparison of experimental results with dynamic model, adapted with permission from Ref. (Grohn et al., 2022a). Copyright: (2022) Elsevier B.V.

Fig. 25 shows the maximum liquid bridge length between two particles and in particle–wall contact. The experiments performed using the pneumatic cylinder setup at different collision velocities are compared with the dynamic model in **Eqns. (27)** and **(28)**, with $C_{pp} = 6.266\,\frac{s}{m}$ and $C_{pw} = 4.424\,\frac{s}{m}$ (Grohn et al., 2022a).

The collision velocity and contact surface curvature of the contact partners showed strong effects on the maximum liquid bridge length, which can be well predicted by the dynamic model. This model implemented in DEM could predict wet particle dynamics in a fluidized bed rotor granulator (Grohn et al., 2022b).

The shape of the liquid bridge that defines the curvature of the liquid–gas–solid interface is often approximated as parabolic by two principal radii (Lian et al., 1993; Mikami et al., 1998; Rabinovich et al., 2005). The collision dynamics of particles may cause a deviation from this shape as the bridge is stretched due to inertia, leading to an elongation of the central part of the bridge before the bridge ruptures (Antonyuk et al., 2009). Grohn et al. (2022a) proposed an alternative approximation of the shape as a set of three trapezoids rotated around a symmetry axis representing the upper, lower, and central parts of the bridge (**Fig. 22 right**).

3.3.4 Direct measurement of fluid-induced forces

For the experimental validation of models that describe the forces acting on the interacting particles from the liquid, it is possible to measure these forces directly.

Pitois et al. (2001) developed an apparatus specifically designed to measure the dynamic forces in a liquid bridge stretched between two particles. The dependence of the liquid bridge force on the separation velocity was described by a model that considers the capillary and lubrication forces.

The so-called “colloidal probe technique” uses an atomic force microscope with a particle attached to the cantilever for measuring the capillary forces in liquid bridges (Kappl and Butt, 2002; Rabinovich et al., 2005). These experiments are static measurements because no velocity variation is applied or the velocity is low enough

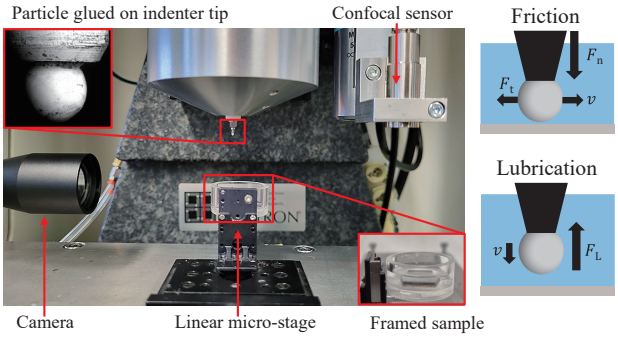

Fig. 26 Extended nanoindentation setup for measuring lubrication and friction forces between a particle and its surface.

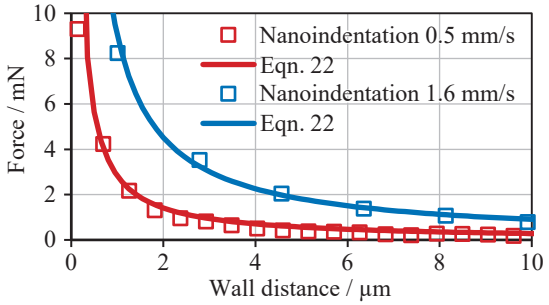

Fig. 27 Measurement of the lubrication force of 900 µm zirconium oxide particles on a polished titanium substrate in glycerol at different velocities compared with **Eqn. (22)**, adapted with permission from Ref. (Strohner and Antonyuk, 2023). Copyright: (2023) Elsevier B.V.

to be neglected. Consequently, the static nature of the experiment also prevents the measurement of the lubrication force during the particle approach. This problem can be solved by the extended nanoindentation setup shown in **Fig. 26**.

The examined substrate sample was covered with liquid in a container placed on the linear microstage. A linear unit (maximum velocity of 1.6 mm/s) was used to move the sample toward a particle attached to the indenter tip. The lubrication force and the distance between the particle and surface were measured directly during the approach. **Fig. 27** shows the results of lubrication force measurements between a zirconia particle and a polished titanium surface completely immersed in glycerol at different velocities. The good agreement between the measured force-distance relationships and the model in **Eqn. (22)** validates the proposed method (Strohner and Antonyuk, 2023).

The load cell of the nanoindenter device can measure forces in the normal and tangential directions. The influence of the liquid layer on the friction coefficients of single particles can be measured by moving the substrate on the linear unit in the tangential direction at a constant normal force. **Fig. 28** compares the friction forces in dry and wet contacts for zirconia particles on a microstructured titanium surface at a normal force of 1 N. For wet friction, a 100 µm layer of silicon oil was applied to the surface.

3.3.5 Investigation of moisture-dependent particle properties

The determination of the mechanical material parameters of moist particles or agglomerates requires a controlled experimental environment to ensure consistent climatic conditions because these can influence the saturation degree and thus the mechanical behavior of the particles (Antonyuk et al., 2015; Mueller et al., 2011). Therefore, mechanical tests of moist particles are usually performed in a climatic chamber to prevent drying (Grohn et al., 2020; Weis et al., 2019).

The compression tests can be used to investigate how Young's modulus, stiffness, yield, and compression strength are affected by the moisture content of the particles. **Fig. 29** shows the typical loading–unloading curves measured in compression tests of wet and dry pharmaceutical spherical particles in the size range of 1.0–1.2 mm. The pellets were produced via an extrusion–spheronization process from 20 wt% microcrystalline cellulose and 80 wt% of α-lactose monohydrate with the addition of conserved water (Weis et al., 2019). The moisture content (weight of water related to the total mass) was measured using a moisture analyzer (MA100, Sartorius) for the wet particles at $0.287 \pm 5 \times 10^{-3}$ g/g and at $9.690 \times 10^{-3} \pm 4 \times 10^{-4}$ g/g after drying. The compression tests of the wet particles were performed using a Texture Analyzer inside a climatic chamber at a relative humidity of 90–95 %. The linear slope of the load curve indicates the dominant plastic behavior of wet and dry particles according to the model in **Eqn. (13)**, which is confirmed by the large plastic deformation after unloading. The model for the unloading force in **Eqn. (15)** and the resulting plastic deformation in **Eqn. (18)** can accurately predict the experimental results. During unloading, the curve of the wet particles shows adhesion due to the liquid bridge formed by the squeezed liquid. This adhesion force can be considered in the DEM as an additional capillary force in the contact model (Weis et al., 2021). The difference in the slope of the loading curves shows that the wet particles exhibit a significantly lower plastic stiffness and a correspondingly higher deformation than the dry particles, despite being exposed to much lower forces. According to the model in **Eqn. (13)**, the obtained yield pressure of wet particles is $p_{y,wet} = 0.31 \pm 0.05$ MPa, which is much lower than the dry state ($p_{y,dry} = 52.6 \pm 14.1$ MPa).

The influence of dynamic effects, such as viscous forces, on the deformation mechanisms of wet particles can be studied using collision tests. The use of a climatic chamber in such experiments is also often necessary to maintain a constant moisture content in the particles. In some studies, impact tests have shown that ambient humidity affects the capillary forces in contact (see humidity-dependent CoR (Li et al., 2019)).

The coefficients of restitution for wet and dry pharmaceutical particles described in previous compression tests are shown in **Fig. 30**. The measurements were performed in a climatic chamber designed for a free fall collision setup (Weis et al., 2019). The CoR of dry particles decreased with increasing velocity because of the increased plastic deformation. The moisture of particles significantly reduces CoR owing to viscous and capillary effects. At impact velocities lower than the sticking velocity ($v < v_s = 0.36$ m/s), the wet particles adhere to the surface because of the formation of a liquid bridge in the contact. As the impact velocity increases, the adhesive force is overcome by higher impact energy and the particle rebounds. Although the CoR increased, its maximum value at $v = 0.86$ m/s was still much smaller than the CoR of dry particles. A further

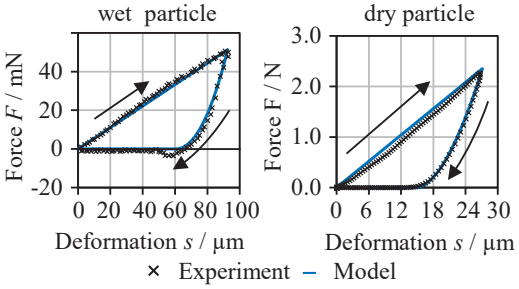

Fig. 29 Force–displacement curves of dry and wet pharmaceutical particles were measured and described using **Eqns. (13)** and **(15)**, adapted with permission from Ref. (Weis et al., 2019). Copyright: (2019) Elsevier B.V.

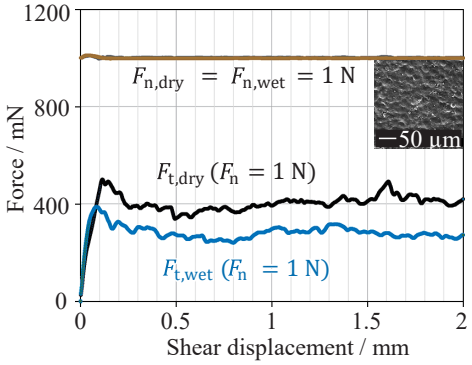

Fig. 28 Friction measurement of zirconium oxide particles ($d = 912$ µm) on a microstructured titanium surface, dry, and covered by a 100 µm layer of silicon oil.

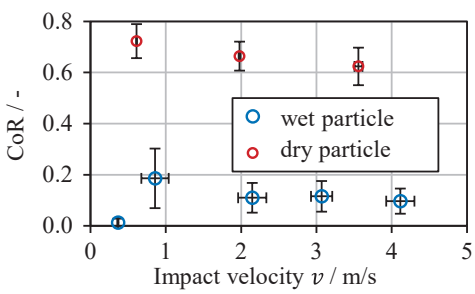

Fig. 30 The CoR of dry and wet pharmaceutical particles was measured using free fall tests, adapted with permission from Ref. (Weis et al., 2019). Copyright: (2019) Elsevier B.V.

increase in impact velocity decreases CoR. In addition to plastic deformation, various effects can contribute to this increase in energy dissipation, e.g., liquid squeezing out of the porous particles leads to viscous deformation behavior and the formation of larger capillary bridges in the contact.

3.4 Bulk experiments for DEM validation of wetted and immersed systems

Similar to the validation of DEM models for dry particle systems (**Section 2.2.3**), bulk measurement methods can be developed that are suitable for wetted and immersed particles. Tests with small amounts of particles are advantageous for quickly calibrating parameters before the simulation of the entire process is performed.

The measurement of the AoR, which is realized for dry bulk materials using a hopper, should be performed for wetted particles with a lifting cylinder setup because the flow through a hopper can become difficult due to strong capillary forces between the particles, resulting in high cohesion and poor flowability. However, instead of a particle pile, a cylindrical shape can remain, depending on the liquid content, as shown in **Fig. 31 (top)** for the spherical 1-mm glass beads. The comparison of the shape and the diameter-to-height ratio was used to validate the DEM model. In addition, the dynamic AoR can be measured using a rotating drum, as shown in **Fig. 31 (bottom)**. By adding a liquid at a low concentration (1 wt%), the dynamic AoR increased compared with the dry experiments (compare with **Fig. 14**) due to the capillary force of the wetted particles.

The influence of the liquid content on the friction and cohesion can be investigated using shear cells and a powder rheometer, as in the dry case (Wittel et al., 2019). In addition, the shear box test and draw-down test can be performed using wetted particles (Carr et al., 2023).

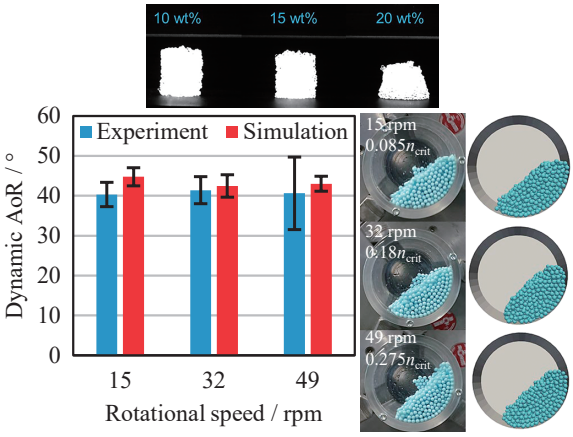

Fig. 31 Static and dynamic AoR of wetted particles. **Top**: 1 mm glass beads with water content variation. **Bottom**: Rotating a drum coated with zirconium oxide particles (3 mm) and 1 wt% water compared with a simulation using the Hertz–Mindlin model with the liquid bridge model.

The dynamic spreading behavior of wetted particle systems can be investigated using vibration experiments. By creating a pile on a vibration shaker (**Fig. 32 top**), the collapse of the pile as a function of amplitude and frequency can be recorded by a camera and used to validate the DEM model by comparing the change in height and spreading diameter over time. **Fig. 32** shows the spreading behavior of glass beads (diameter of 1.1 mm) with a water content of 15 wt% at different amplitudes at 69 Hz. The liquid bridge model described in **Section 3.1.2** was implemented in the DEM. The simulations showed good agreement with the experiments over the investigated period. With increasing amplitude, the pile collapsed faster, and at an amplitude of 156 µm, a constant height was achieved after 20 s.

Wetted and sticky particle systems, e.g., pastes, can be studied using an extrusion setup to validate the DEM simulation with the flow behavior of the material under different compression and shear stresses. During vertical movement, the punch presses the material out of the mold. The normal force needed to extrude the wet particle system and the displacement of the punch were measured. The resulting force–displacement curve of the extrusion process can be used to calibrate the friction and adhesion parameters in the DEM model.

The validation of the DEM model for a particle system suspended in liquid is more difficult to realize because the fluid flow–particle interactions complicate the simulations. The AoR in liquid can be determined by immersing the whole experimental setup to prevent the influence of air and excessive fluid flow through particle sedimentation.

The initial step involves positioning the cylinder (7 mm inner diameter with an outlet of 2 mm) and bottom plate inside a container filled with water. Subsequently, the particles were suspended inside the cylinder using a funnel with an opening situated close to the bottom plate to reduce the classification effect during sedimentation. Once the particles had settled to the base of the cylinder, the cylinder was slowly elevated in order to minimize the impact of the flow

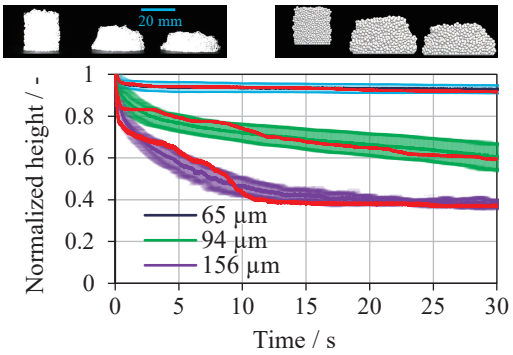

Fig. 32 Spreading behavior of wetted glass beads with a water content of 15 wt% at 69 Hz with different amplitudes. The DEM results (red curve) were obtained using Hertz–Mindlin model with a liquid bridge model according to Grohn et al. (2022a).

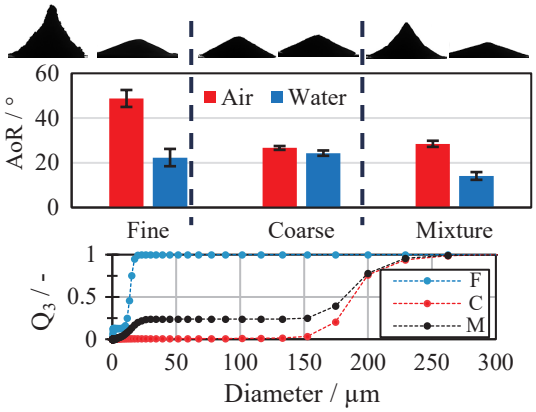

Fig. 33 Comparison of the AoR values of glass beads in air and water. Q_3 refers to the particle size distribution.

effects on the AoR within the fluid. **Fig. 33** shows a comparison of the AoR measured in air and water for glass beads with a constant sample mass of 1 g and varying particle size distribution, where the mixture (M) is a 27:73 w% combination of fine (F) and coarse (C) fractions. The reduction in friction and cohesion in water was evident in the fine and mixed samples, as indicated by the decrease in pile height and AoR. In water, gravitation had a more dominant effect on these fractions than cohesion. Consequently, in contrast to air, the impact of the studied particle sizes in water on the pile shape and AoR is not significant.

4. Conclusion

The Discrete Element Method represents a significant advancement in the field of particulate processes, offering a comprehensive and accurate numerical description. The application of more accurate measurements or calibrations of the model parameters will result in more precise predictions of the interactions within a real particle system using the DEM. This paper presents a review of the methods used to measure contact model parameters.

Single-particle tests, such as nanoindentation, can be employed to determine the mechanical properties and validate contact models. As particles within a bulk material often exhibit complex multi-contact loading scenarios, it is sometimes necessary to calibrate parameters measured by single particle tests using bulk methods.

While some methods have been established for measuring dry particles, only a few are currently available for wet particles, particles with liquid layers, and particles immersed in liquid. Liquid bridges and layers can be investigated by impact and shear tests in the presence of liquid layers. The influence of the impact velocity on the restitution and friction coefficients, as well as the geometry and rupture length of liquid bridges, must often be considered because of dominant dynamic forces. The deformation and breakage behaviors of moist particles are strongly influenced by moisture content and stress rate.

Impact tests and nanoindentation with particles fixed on the indenter tip can be used to investigate the contact behavior in the liquid. The measured parameters, such as CoR, AoR, and friction coefficient, frequently exhibit a significant deviation from the dry case. Consequently, these parameters must be modified in contact models to account for deviations.

The suitability of individual measurement methods is determined by the range of forces, deformations, and velocities, and the methods must be adapted to the specific conditions of the investigated process.

Nomenclature

AFM	Atomic force microscopy
AoR	Angle of repose
CFD	Computational fluid dynamics
CoR	Coefficient of restitution
DEM	Discrete element method
PSD	Particle size distribution
SPM	Scanning probe microscopy
pp	particle–particle
pw	particle–wall
C_{pp}, C_{pw}	constant parameters of liquid bridge ($s \cdot m^{-1}$)
d_p	particle diameter (m)
e	coefficient of restitution (-)
E_{kin}	kinetic energy (J)
E^*	equivalent modulus of elasticity (Pa)
F	force (N)
F_y	yield force (N)
h	wall distance (m)
h_{init}	initial lubrication height (m)
h_{min}	limiting height of lubrication (m)
J	moment of inertia ($kg \cdot m^2$)
l_{max}	maximum liquid bridge length (m)
m_p	particle mass (kg)
M	torque (Nm)
p	pressure (Pa)
p_y	yield pressure (Pa)
R	radius (m)
R^*	equivalent radius (m)
r_c	contact radius (m)
s_r	roughness parameter for lubrication force (m)
s_{max}	maximum deformation (m)
s_y	yield deformation (m)
St	Stokes number (-)
v	velocity ($m \cdot s^{-1}$)
V	volume (m^3)
γ	surface tension (mN/m)
η_f	viscosity (Pa·s)
θ	contact angle (°)
φ	moisture content (-)
ρ	density ($kg \cdot m^{-3}$)

References

Abi-Mansour A., McClure S., Gentzler M., XRCT characterization of mesoscopic structure in poured and tapped cohesive powders and prediction by DEM, Powder Technology, 330 (2018) 386–396. https://doi.org/10.1016/j.powtec.2018.01.081

Adams M.J., Lawrence C.J., Urso M., Rance J., Modelling collisions of soft agglomerates at the continuum length scale, Powder Technology, 140 (2004) 268–279. https://doi.org/10.1016/j.powtec.2004.01.013

Adams M.J., Perchard V., The cohesive forces between particles with interstitial liquid, Institution of Chemical Engineering Symposium Series, 91 (1985) 147–160.
Alizadeh M., Hassanpour A., Pasha M., Ghadiri M., Bayly A., The effect of particle shape on predicted segregation in binary powder mixtures, Powder Technology, 319 (2017) 313–322. https://doi.org/10.1016/j.powtec.2017.06.059
Amoozegar A., Heitman J.L., Kranz C.N., Comparison of soil particle density determined by a gas pycnometer using helium, nitrogen, and air, Soil Science Society of America Journal, 87 (2023) 1–12. https://doi.org/10.1002/saj2.20476
Angus A., Yahia L.A.A., Maione R., Khala M., Hare C., Ozel A., Ocone R., Calibrating friction coefficients in discrete element method simulations with shear-cell experiments, Powder Technology, 372 (2020) 290–304. https://doi.org/10.1016/j.powtec.2020.05.079
Antonyuk S., Heinrich S., Deen N., Kuipers H., Influence of liquid layers on energy absorption during particle impact, Particuology, 7 (2009) 245–259. https://doi.org/10.1016/j.partic.2009.04.006
Antonyuk S., Heinrich S., Gurikov P., Raman S., Smirnova I., Influence of coating and wetting on the mechanical behaviour of highly porous cylindrical aerogel particles, Powder Technology, 285 (2015) 34–43. https://doi.org/10.1016/j.powtec.2015.05.004
Antonyuk S., Heinrich S., Tomas J., Deen N.G., van Buijtenen M.S., Kuipers J.A.M., Energy absorption during compression and impact of dry elastic-plastic spherical granules, Granular Matter, 12 (2010) 15–47. https://doi.org/10.1007/s10035-009-0161-3
Aurich J.C., Altherr N., Kieren-Ehses S., Kirsch B., Mayer T., Creating surface morphologies by micro milling and micro grinding, in: Aurich J.C., Hasse H. (Eds.), Component Surfaces, Springer International Publishing, Cham, 2024, ISBN:9783031355745, pp. 67–95. https://doi.org/10.1007/978-3-031-35575-2
Bagheri G.H., Bonadonna C., Manzella I., Vonlanthen P., On the characterization of size and shape of irregular particles, Powder Technology, 270 (2015) 141–153. https://doi.org/10.1016/j.powtec.2014.10.015
Barnocky G., Davis R.H., Elastohydrodynamic collision and rebound of spheres: experimental verification, The Physics of Fluids, 31 (1988) 1324–1329. https://doi.org/10.1063/1.866725
Barrett E.P., Joyner L.G., Halenda P.P., The determination of pore volume and area distributions in porous substances. I. computations from nitrogen isotherms, Journal of the American Chemical Society, 73 (1951) 373–380. https://doi.org/10.1021/ja01145a126
Bhattad A., Review on viscosity measurement: devices, methods and models, Journal of Thermal Analysis and Calorimetry, 148 (2023) 6527–6543. https://doi.org/10.1007/s10973-023-12214-0
Bilz R., de Payrebrune K.M., Investigation of the influence of velocity in a tribological three-body system containing a single layer of rolling hard particles from a mechanical point of view, Tribology International, 159 (2021) 106948. https://doi.org/10.1016/j.triboint.2021.106948
Breuninger P., Weis D., Behrendt I., Grohn P., Krull F., Antonyuk S., CFD–DEM simulation of fine particles in a spouted bed apparatus with a Wurster tube, Particuology, 42 (2019) 114–125. https://doi.org/10.1016/j.partic.2018.03.015
Brilliantov N.V., Spahn F., Hertzsch J.M., Pöschel T., Model for collisions in granular gases, Physical Review E, 53 (1996) 5382–5392. https://doi.org/10.1103/PhysRevE.53.5382
Buck B., Tang Y., Deen N.G., Kuipers J., Heinrich S., Dynamics of wet particle–wall collisions: Influence of wetting condition, Chemical Engineering Research and Design, 135 (2018) 21–29. https://doi.org/10.1016/j.cherd.2018.05.014
Bunke F., Pietsch-Braune S., Heinrich S., Three-dimensional measurement method of binary particle collisions under dry and wet conditions, Chemical Engineering Journal, 489 (2024) 151016. https://doi.org/10.1016/j.cej.2024.151016
Burmeister C.F., Hofer M., Molaiyan P., Michalowski P., Kwade A., Characterization of stressing conditions in a high energy ball mill by discrete element simulations, Processes, 10 (2022) 692. https://doi.org/10.3390/pr10040692
Butt H.-J., Cappella B., Kappl M., Force measurements with the atomic force microscope: technique, interpretation and applications, Surface Science Reports, 59 (2005) 1–152. https://doi.org/10.1016/j.surfrep.2005.08.003
Butt H.-J., Liu J., Koynov K., Straub B., Hinduja C., Roismann I., Berger R., Li X., Vollmer D., Steffen W., Kappl M., Contact angle hysteresis, Current Opinion in Colloid & Interface Science, 59 (2022) 101574. https://doi.org/10.1016/j.cocis.2022.101574
Carr M.J., Roessler T., Robinson P.W., Otto H., Richter C., Katterfeld A., Wheeler C.A., Calibration procedure of Discrete Element Method (DEM) parameters for wet and sticky bulk materials, Powder Technology, 429 (2023) 118919. https://doi.org/10.1016/j.powtec.2023.118919
Cleary P.W., Large scale industrial DEM modelling, Engineering Computations, 21 (2004) 169–204. https://doi.org/10.1108/02644400410519730
Coetzee C., Calibration of the discrete element method: strategies for spherical and non-spherical particles, Powder Technology, 364 (2020) 851–878. https://doi.org/10.1016/j.powtec.2020.01.076
Coetzee C.J., Review: calibration of the discrete element method, Powder Technology, 310 (2017) 104–142. https://doi.org/10.1016/j.powtec.2017.01.015
Coetzee C.J., Particle upscaling: calibration and validation of the discrete element method, Powder Technology, 344 (2019) 487–503. https://doi.org/10.1016/j.powtec.2018.12.022
Coetzee C.J., Els D., Calibration of discrete element parameters and the modelling of silo discharge and bucket filling, Computers and Electronics in Agriculture, 65 (2009) 198–212. https://doi.org/10.1016/j.compag.2008.10.002
Coetzee C.J., Scheffler O.C., Review: the calibration of DEM parameters for the bulk modelling of cohesive materials, Processes, 11 (2023) 5. https://doi.org/10.3390/pr11010005
Crüger B., Heinrich S., Antonyuk S., Deen N.G., Kuipers J., Experimental study of oblique impact of particles on wet surfaces, Chemical Engineering Research and Design, 110 (2016a) 209–219. https://doi.org/10.1016/j.cherd.2016.01.024
Crüger B., Salikov V., Heinrich S., Antonyuk S., Sutkar V.S., Deen N.G., Kuipers J., Coefficient of restitution for particles impacting on wet surfaces: an improved experimental approach, Particuology, 25 (2016b) 1–9. https://doi.org/10.1016/j.partic.2015.04.002
Cundall P.A., Strack O.D.L., A discrete numerical model for granular assemblies, Géotechnique, 29 (1979) 47–65. https://doi.org/10.1680/geot.1979.29.1.47
Cunha R.N., Santos K.G., Lima R.N., Duarte C.R., Barrozo M., Repose angle of monoparticles and binary mixture: an experimental and simulation study, Powder Technology, 303 (2016) 203–211. https://doi.org/10.1016/j.powtec.2016.09.023
Davis R.H., Rager D.A., Good B.T., Elastohydrodynamic rebound of spheres from coated surfaces, Journal of Fluid Mechanics, 468 (2002) 107–119. https://doi.org/10.1017/S0022112002001489
Deen N.G., van Sint Annaland M., van der Hoef M.A., Kuipers J., Review of discrete particle modeling of fluidized beds, Chemical Engineering Science, 62 (2007) 28–44. https://doi.org/10.1016/j.ces.2006.08.014
Deshpande R., Antonyuk S., Iliev O., Study of the filter cake formed due to the sedimentation of monodispersed and bidispersed particles using discrete element method–computational fluid dynamics simulations, AIChE Journal, 65 (2019) 1294–1303. https://doi.org/10.1002/aic.16529
Deshpande R., Antonyuk S., Iliev O., DEM-CFD study of the filter cake formation process due to non-spherical particles, Particuology, 53 (2020) 48–57. https://doi.org/10.1016/j.partic.2020.01.003
Di Maio F.P., Di Renzo A., DEM-CFD simulations of fluidized beds with application in mixing dynamics, KONA Powder and Particle Journal, 25 (2007) 205–216. https://doi.org/10.14356/kona.2007018
Ditscherlein R., Furat O., Langlard M. de, Martins de Souza E Silva J., Sygusch J., Rudolph M., Leißner T., Schmidt V., Peuker U.A., Multiscale tomographic analysis for micron-sized particulate samples, Microscopy and Microanalysis, 26 (2020) 676–688. https://doi.org/10.1017/S1431927620001737
Dong H., Moys M.H., Experimental study of oblique impacts with initial

spin, Powder Technology, 161 (2006) 22–31. https://doi.org/10.1016/j.powtec.2005.05.046
Dong M., Li X., Mei Y., Li S., Experimental and theoretical analyses on the effect of physical properties and humidity of fly ash impacting on a flat surface, Journal of Aerosol Science, 117 (2018) 85–99. https://doi.org/10.1016/j.jaerosci.2017.12.012
Dosta M., Dale S., Antonyuk S., Wassgren C., Heinrich S., Litster J.D., Numerical and experimental analysis of influence of granule microstructure on its compression breakage, Powder Technology, 299 (2016) 87–97. https://doi.org/10.1016/j.powtec.2016.05.005
Endres S.C., Ciacchi L.C., Mädler L., A review of contact force models between nanoparticles in agglomerates, aggregates, and films, Journal of Aerosol Science, 153 (2021) 105719. https://doi.org/10.1016/j.jaerosci.2020.105719
Ennis B.J., Tardos G., Pfeffer R., A microlevel-based characterization of granulation phenomena, Powder Technology, 65 (1991) 257–272. https://doi.org/10.1016/0032-5910(91)80189-P
Fischer-Cripps A.C., Nicholson D.W., Nanoindentation. Mechanical engineering series, Applied Mechanics Reviews, 57 (2004) 145–160. https://doi.org/10.1115/1.1704625
Forgber T., Khinast J.G., Fink E., A hybrid workflow for investigating wide DEM parameter spaces, Powder Technology, 404 (2022) 117440. https://doi.org/10.1016/j.powtec.2022.117440
Franses E.I., Basaran O.A., Chang C.-H., Techniques to measure dynamic surface tension, Current Opinion in Colloid & Interface Science, 1 (1996) 296–303. https://doi.org/10.1016/S1359-0294(96)80018-5
Fries L., Antonyuk S., Heinrich S., Palzer S., DEM–CFD modeling of a fluidized bed spray granulator, Chemical Engineering Science, 66 (2011) 2340–2355. https://doi.org/10.1016/j.ces.2011.02.038
Fu J., Adams M.J., Reynolds G.K., Salman A.D., Hounslow M.J., Impact deformation and rebound of wet granules, Powder Technology, 140 (2004) 248–257. https://doi.org/10.1016/j.powtec.2004.01.012
Fuchs R., Weinhart T., Meyer J., Zhuang H., Staedler T., Jiang X., Luding S., Rolling, sliding and torsion of micron-sized silica particles: experimental, numerical and theoretical analysis, Granular Matter, 16 (2014) 281–297. https://doi.org/10.1007/s10035-014-0481-9
Gao Y., Simone G. de, Koorapaty M., Calibration and verification of DEM parameters for the quantitative simulation of pharmaceutical powder compression process, Powder Technology, 378 (2021) 160–171. https://doi.org/10.1016/j.powtec.2020.09.019
Ge R., Boyce A.M., Shui Zhang Y., Shearing P.R., Cumming D.J., Smith R.M., Discrete element method and electrochemical modelling of lithium ion cathode structures characterised by X-ray computed tomography, Chemical Engineering Journal, 465 (2023) 142749. https://doi.org/10.1016/j.cej.2023.142749
Giannis K., Kwade A., Finke J.H., Schilde C., The effect of particle shape on the compaction of realistic non-spherical particles-a multi-contact dem study, Pharmaceutics, 15 (2023) 909. https://doi.org/10.3390/pharmaceutics15030909
Goldman A.J., Cox R.G., Brenner H., Slow viscous motion of a sphere parallel to a plane wall—I Motion through a quiescent fluid, Chemical Engineering Science, 22 (1967) 637–651. https://doi.org/10.1016/0009-2509(67)80047-2
Gollwitzer F., Rehberg I., Kruelle C.A., Huang K., Coefficient of restitution for wet particles, Physical Review E, 86 (2012) 11303. https://doi.org/10.1103/PhysRevE.86.011303
Golshan S., Sotudeh-Gharebagh R., Zarghami R., Mostoufi N., Blais B., Kuipers J., Review and implementation of CFD-DEM applied to chemical process systems, Chemical Engineering Science, 221 (2020) 115646. https://doi.org/10.1016/j.ces.2020.115646
Götzinger M., Peukert W., Dispersive forces of particle–surface interactions: direct AFM measurements and modelling, Powder Technology, 130 (2003) 102–109. https://doi.org/10.1016/S0032-5910(02)00234-6
Grima A.P., Wypych P.W., Development and validation of calibration methods for discrete element modelling, Granular Matter, 13 (2011) 127–132. https://doi.org/10.1007/s10035-010-0197-4
Grohn P., Heinrich S., Antonyuk S., Numerical investigation of the particle dynamics in a rotorgranulator depending on the properties of the coating liquid, Pharmaceutics, 15 (2023a) 469. https://doi.org/10.3390/pharmaceutics15020469
Grohn P., Oesau T., Heinrich S., Antonyuk S., Investigation of the influence of impact velocity and liquid bridge volume on the maximum liquid bridge length, Advanced Powder Technology, 33 (2022a) 103630. https://doi.org/10.1016/j.apt.2022.103630
Grohn P., Oesau T., Heinrich S., Antonyuk S., Investigation of the influence of wetting on the particle dynamics in a fluidized bed rotor granulator by MPT measurements and CFD-DEM simulations, Powder Technology, 408 (2022b) 117736. https://doi.org/10.1016/j.powtec.2022.117736
Grohn P., Schaedler L., Atxutegi A., Heinrich S., Antonyuk S., CFD-DEM simulation of superquadric cylindrical particles in a spouted bed and a rotor granulator, Chemie Ingenieur Technik, 95 (2023b) 244–255. https://doi.org/10.1002/cite.202200121
Grohn P., Weis D., Thommes M., Heinrich S., Antonyuk S., Contact behavior of microcrystalline cellulose pellets depending on their water content, Chemical Engineering & Technology, 43 (2020) 887–895. https://doi.org/10.1002/ceat.201900517
Guo Y., Wu C.-Y., Kafui K.D., Thornton C., 3D DEM/CFD analysis of size-induced segregation during die filling, Powder Technology, 206 (2011) 177–188. https://doi.org/10.1016/j.powtec.2010.05.029
Hadi A., Roeplal R., Pang Y., Schott D.L., DEM modelling of segregation in granular materials: a review, KONA Powder and Particle Journal, 41 (2024) 78–107. https://doi.org/10.14356/kona.2024017
Han F., Ganju E., Salgado R., Prezzi M., Effects of interface roughness, particle geometry, and gradation on the sand–steel interface friction angle, Journal of Geotechnical and Geoenvironmental Engineering, 144 (2018) 04018096. https://doi.org/10.1061/(ASCE)GT.1943-5606.0001990
Handl L., Torbahn L., Spettl A., Schmidt V., Kwade A., Structural analysis and tracking of micron-sized glass particles during shear deformation: a study based on time-resolved tomographic data, Advanced Powder Technology, 28 (2017) 1920–1929. https://doi.org/10.1016/j.apt.2017.05.002
Härtl J., Ooi J.Y., Numerical investigation of particle shape and particle friction on limiting bulk friction in direct shear tests and comparison with experiments, Powder Technology, 212 (2011) 231–239. https://doi.org/10.1016/j.powtec.2011.05.022
Hayashi K., Nakamura H., Watano S., Numerical study on granule aggregation and breakage in fluidized bed granulation by a novel PBM with DEM-CFD coupling approach, Powder Technology, 360 (2020) 1321–1336. https://doi.org/10.1016/j.powtec.2019.11.027
Herminghaus S., Semprebon C., Brinkmann M., Capillary Interaction in Wet Granular Assemblies: Part 1, in: Antonyuk S. (Ed.), Particles in Contact, Springer International Publishing, Cham, 2019, ISBN: 9783030158989, pp. 239–275. https://doi.org/10.1007/978-3-030-15899-6_8
Hertz H., Ueber die Berührung fester elastischer Körper, Journal für die reine und angewandte Mathematik, 92 (1882) 156–171. https://doi.org/10.1515/crll.1882.92.156
Hesse R., Krull F., Antonyuk S., Experimentally calibrated CFD-DEM study of air impairment during powder discharge for varying hopper configurations, Powder Technology, 372 (2020) 404–419. https://doi.org/10.1016/j.powtec.2020.05.113
Hesse R., Krull F., Antonyuk S., Prediction of random packing density and flowability for non-spherical particles by deep convolutional neural networks and Discrete Element Method simulations, Powder Technology, 393 (2021) 559–581. https://doi.org/10.1016/j.powtec.2021.07.056
Hesse R., Lösch P., Antonyuk S., CFD-DEM analysis of internal packing structure and pressure characteristics in compressible filter cakes using a novel elastic–plastic contact model, Advanced Powder Technology, 34 (2023) 104062. https://doi.org/10.1016/j.apt.2023.104062
Hlosta J., Žurovec D., Rozbroj J., Ramírez-Gómez Á., Nečas J., Zegzulka J., Experimental determination of particle–particle restitution coefficient via double pendulum method, Chemical Engineering Research and Design, 135 (2018) 222–233. https://doi.org/10.1016/j.cherd.2018.05.016
Hodges C.S., Cleaver J.A.S., Ghadiri M., Jones R., Pollock H.M., Forces

between polystyrene particles in water using the AFM: pull-off force vs particle size, Langmuir: the ACS Journal of Surfaces and Colloids, 18 (2002) 5741–5748. https://doi.org/10.1021/la025604q

Horváth G., Kawazoe K., Method for the calculation of effective pore size distribution in molecular sieve carbon, Journal of Chemical Engineering of Japan, 16 (1983) 470–475. https://doi.org/10.1252/jcej.16.470

Hoshishima C., Ohsaki S., Nakamura H., Watano S., Parameter calibration of discrete element method modelling for cohesive and non-spherical particles of powder, Powder Technology, 386 (2021) 199–208. https://doi.org/10.1016/j.powtec.2021.03.044

Israelachvili J.N., Intermolecular and Surface Forces, third ed., Elsevier Science, Burlington, 2011, ISBN: 9780123919274. https://doi.org/10.1016/C2011-0-05119-0

Iveson S.M., Beathe J.A., Page N.W., The dynamic strength of partially saturated powder compacts: the effect of liquid properties, Powder Technology, 127 (2002) 149–161. https://doi.org/10.1016/S0032-5910(02)00118-3

Iveson S.M., Litster J.D., Hapgood K., Ennis B.J., Nucleation, growth and breakage phenomena in agitated wet granulation processes: a review, Powder Technology, 117 (2001) 3–39. https://doi.org/10.1016/S0032-5910(01)00313-8

Jain D., Deen N.G., Kuipers J., Antonyuk S., Heinrich S., Direct numerical simulation of particle impact on thin liquid films using a combined volume of fluid and immersed boundary method, Chemical Engineering Science, 69 (2012) 530–540. https://doi.org/10.1016/j.ces.2011.11.018

Jajcevic D., Siegmann E., Radeke C., Khinast J.G., Large-scale CFD–DEM simulations of fluidized granular systems, Chemical Engineering Science, 98 (2013) 298–310. https://doi.org/10.1016/j.ces.2013.05.014

Jasevičius R., Baronas R., Kruggel-Emden H., Numerical modelling of the normal adhesive elastic–plastic interaction of a bacterium, Advanced Powder Technology, 26 (2015) 742–752. https://doi.org/10.1016/j.apt.2015.04.010

Ji S., Wang S., Zhou Z., Influence of particle shape on mixing rate in rotating drums based on super-quadric DEM simulations, Advanced Powder Technology, 31 (2020) 3540–3550. https://doi.org/10.1016/j.apt.2020.06.040

Ji X., Chen Y., Hou Y., Dai C., Chen B., Zou H., Surface microscopic properties of various aggregates using laser scanning confocal microscope, Construction and Building Materials, 290 (2021) 123222. https://doi.org/10.1016/j.conbuildmat.2021.123222

Johnson K.L., Contact Mechanics, Cambridge University Press, Cambridge, 1987, ISBN: 9780521347969.

Johnson K.L., Pollock H.M., The role of adhesion in the impact of elastic spheres, Journal of Adhesion Science and Technology, 8 (1994) 1323–1332. https://doi.org/10.1163/156856194X00636

Jones R., From single particle AFM studies of adhesion and friction to bulk flow: forging the links, Granular Matter, 4 (2003) 191–204. https://doi.org/10.1007/s10035-002-0122-6

Joseph G.G., Zenit R., Hunt M.L., Rosenwinkel A.M., Particle–wall collisions in a viscous fluid, Journal of Fluid Mechanics, 433 (2001) 329–346. https://doi.org/10.1017/S0022112001003470

Kappl M., Butt H.-J., The Colloidal probe technique and its application to adhesion force measurements, Particle & Particle Systems Characterization, 19 (2002) 129–143. https://doi.org/10.1002/1521-4117(200207)19:3<129::AID-PPSC129>3.0.CO;2-G

Ketterhagen W., Wassgren C., A perspective on calibration and application of DEM models for simulation of industrial bulk powder processes, Powder Technology, 402 (2022) 117301. https://doi.org/10.1016/j.powtec.2022.117301

Kharaz A.H., Gorham D.A., Salman A.D., An experimental study of the elastic rebound of spheres, Powder Technology, 120 (2001) 281–291. https://doi.org/10.1016/S0032-5910(01)00283-2

Khazeni A., Mansourpour Z., Influence of non-spherical shape approximation on DEM simulation accuracy by multi-sphere method, Powder Technology, 332 (2018) 265–278. https://doi.org/10.1016/j.powtec.2018.03.030

Kildashti K., Dong K., Yu A., Contact force models for non-spherical particles with different surface properties: a review, Powder Technology, 418 (2023) 118323. https://doi.org/10.1016/j.powtec.2023.118323

Kruggel-Emden H., Rickelt S., Wirtz S., Scherer V., A study on the validity of the multi-sphere Discrete Element Method, Powder Technology, 188 (2008a) 153–165. https://doi.org/10.1016/j.powtec.2008.04.037

Kruggel-Emden H., Simsek E., Rickelt S., Wirtz S., Scherer V., Review and extension of normal force models for the Discrete Element Method, Powder Technology, 171 (2007) 157–173. https://doi.org/10.1016/j.powtec.2006.10.004

Kruggel-Emden H., Wirtz S., Scherer V., A study on tangential force laws applicable to the discrete element method (DEM) for materials with viscoelastic or plastic behavior, Chemical Engineering Science, 63 (2008b) 1523–1541. https://doi.org/10.1016/j.ces.2007.11.025

Krull F., Hesse R., Breuninger P., Antonyuk S., Impact behaviour of microparticles with microstructured surfaces: experimental study and DEM simulation, Chemical Engineering Research and Design, 135 (2018) 175–184. https://doi.org/10.1016/j.cherd.2018.05.033

Krull F., Mathy J., Breuninger P., Antonyuk S., Influence of the surface roughness on the collision behavior of fine particles in ambient fluids, Powder Technology, 392 (2021) 58–68. https://doi.org/10.1016/j.powtec.2021.06.051

Krull F., Strohner D., Hering-Stratemeier J., Freymann G. von, Antonyuk S., Measurements of micro particle rotation by applying marking points using additive manufacturing tools, Advanced Powder Technology, 34 (2023) 104218. https://doi.org/10.1016/j.apt.2023.104218

Kuwagi K., Takano K., Horio M., The effect of tangential lubrication by bridge liquid on the behavior of agglomerating fluidized beds, Powder Technology, 113 (2000) 287–298. https://doi.org/10.1016/S0032-5910(00)00311-9

Law K.-Y., Zhao H., Surface Wetting—Characterization, Contact Angle, and Fundamentals, Springer International Publishing, Cham, 2016, ISBN:9783319252124. https://doi.org/10.1007/978-3-319-25214-8

Li L., Remmelgas J., van Wachem B.G., Corswant C. von, Folestad S., Johansson M., Rasmuson A., Effect of drag models on residence time distributions of particles in a Wurster fluidized bed: a DEM-CFD study, KONA Powder and Particle Journal, 33 (2016) 264–277. https://doi.org/10.14356/kona.2016008

Li X., Dong M., Jiang D., Li S., Shang Y., The effect of surface roughness on normal restitution coefficient, adhesion force and friction coefficient of the particle-wall collision, Powder Technology, 362 (2020a) 17–25. https://doi.org/10.1016/j.powtec.2019.11.120

Li X., Dong M., Li S., Shang Y., Experimental and theoretical studies of the relationship between dry and humid normal restitution coefficients, Journal of Aerosol Science, 129 (2019) 16–27. https://doi.org/10.1016/j.jaerosci.2018.12.006

Li X., Dong M., Zhang H., Li S., Shang Y., Effect of surface roughness on capillary force during particle-wall impaction under different humidity conditions, Powder Technology, 371 (2020b) 244–255. https://doi.org/10.1016/j.powtec.2020.05.053

Lian G., Thornton C., Adams M.J., A theoretical study of the liquid bridge forces between two rigid spherical bodies, Journal of Colloid and Interface Science, 161 (1993) 138–147. https://doi.org/10.1006/jcis.1993.1452

Lian G., Thornton C., Adams M.J., Discrete particle simulation of agglomerate impact coalescence, Chemical Engineering Science, 53 (1998) 3381–3391. https://doi.org/10.1016/S0009-2509(98)00152-3

Liu L.X., Litster J.D., Iveson S.M., Ennis B.J., Coalescence of deformable granules in wet granulation processes, AIChE Journal, 46 (2000) 529–539. https://doi.org/10.1002/aic.690460312

Lu G., Third J.R., Müller C.R., Discrete element models for non-spherical particle systems: from theoretical developments to applications, Chemical Engineering Science, 127 (2015) 425–465. https://doi.org/10.1016/j.ces.2014.11.050

Luding S., Molecular dynamics simulations of granular materials, in: Hinrichsen H., Wolf D.E. (Eds.), The Physics of Granular Media, Wiley, 2004, ISBN: 9783527403738, pp. 297–324.

https://doi.org/10.1002/352760362X.ch13
Luding S., Introduction to discrete element methods, European Journal of Environmental and Civil Engineering, 12 (2008) 785–826. https://doi.org/10.1080/19648189.2008.9693050
Lv Y., Li X., Fan C., Su Y., Effects of internal pores on the mechanical properties of marine calcareous sand particles, Acta Geotechnica, 16 (2021) 3209–3228. https://doi.org/10.1007/s11440-021-01223-8
Ma H., Zhao Y., Modelling of the flow of ellipsoidal particles in a horizontal rotating drum based on DEM simulation, Chemical Engineering Science, 172 (2017) 636–651. https://doi.org/10.1016/j.ces.2017.07.017
Mader-Arndt K., Aman S., Fuchs R., Tomas J., Contact properties determination of macroscopic fine disperse glass particles via compression tests in normal direction, Advanced Powder Technology, 28 (2017) 101–114. https://doi.org/10.1016/j.apt.2016.09.014
Marigo M., Stitt E.H., Discrete Element Method (DEM) for industrial applications: comments on calibration and validation for the modelling of cylindrical pellets, KONA Powder and Particle Journal, 32 (2015) 236–252. https://doi.org/10.14356/kona.2015016
Markauskas D., Kačianauskas R., Džiugys A., Navakas R., Investigation of adequacy of multi-sphere approximation of elliptical particles for DEM simulations, Granular Matter, 12 (2010) 107–123. https://doi.org/10.1007/s10035-009-0158-y
Matthewson M.J., Adhesion of spheres by thin liquid films, Philosophical Magazine A, 57 (1988) 207–216. https://doi.org/10.1080/01418618808204510
Maw N., Barber J.R., Fawcett J.N., The oblique impact of elastic spheres, Wear, 38 (1976) 101–114. https://doi.org/10.1016/0043-1648(76)90201-5
Megias-Alguacil D., Gauckler L.J., Capillary forces between two solid spheres linked by a concave liquid bridge: regions of existence and forces mapping, AIChE Journal, 55 (2009) 1103–1109. https://doi.org/10.1002/aic.11726
Merkus H.G., Particle Size Measurements—Fundamentals, Practice, Quality, Springer Netherlands, Dordrecht, 2009, ISBN: 9781402090158. https://doi.org/10.1007/978-1-4020-9016-5
Mikami T., Kamiya H., Horio M., Numerical simulation of cohesive powder behavior in a fluidized bed, Chemical Engineering Science, 53 (1998) 1927–1940. https://doi.org/10.1016/S0009-2509(97)00325-4
Mindlin R.D., Deresiewicz H., Elastic spheres in contact under varying oblique forces, Journal of Applied Mechanics, 20 (1953) 327–344. https://doi.org/10.1115/1.4010702
Mohammadi-Jam S., Waters K.E., Inverse gas chromatography applications: a review, Advances in Colloid and Interface Science, 212 (2014) 21–44. https://doi.org/10.1016/j.cis.2014.07.002
Molerus O., Theory of yield of cohesive powders, Powder Technology, 12 (1975) 259–275. https://doi.org/10.1016/0032-5910(75)85025-X
Mongruel A., Gondret P., Viscous dissipation in the collision between a sphere and a textured wall, Journal of Fluid Mechanics, 896 (2020) A8. https://doi.org/10.1017/jfm.2020.325
Mueller P., Antonyuk S., Stasiak M., Tomas J., Heinrich S., The normal and oblique impact of three types of wet granules, Granular Matter, 13 (2011) 455–463. https://doi.org/10.1007/s10035-011-0256-5
Mullier M., Tüzün U., Walton O.R., A single-particle friction cell for measuring contact frictional properties of granular materials, Powder Technology, 65 (1991) 61–74. https://doi.org/10.1016/0032-5910(91)80169-J
Nakashima H., Shioji Y., Kobayashi T., Aoki S., Shimizu H., Miyasaka J., Ohdoi K., Determining the angle of repose of sand under low-gravity conditions using discrete element method, Journal of Terramechanics, 48 (2011) 17–26. https://doi.org/10.1016/j.jterra.2010.09.002
Nijssen T.M., Ottens M., Padding J.T., A note on the modelling of lubrication forces in unresolved simulations, Powder Technology, 413 (2023) 118017. https://doi.org/10.1016/j.powtec.2022.118017
Olsson E., Jelagin D., A contact model for the normal force between viscoelastic particles in discrete element simulations, Powder Technology, 342 (2019) 985–991. https://doi.org/10.1016/j.powtec.2018.10.022
Olsson E., Larsson P.-L., On force–displacement relations at contact between elastic–plastic adhesive bodies, Journal of the Mechanics and Physics of Solids, 61 (2013) 1185–1201. https://doi.org/10.1016/j.jmps.2013.01.004
Owens D.K., Wendt R.C., Estimation of the surface free energy of polymers, Journal of Applied Polymer Science, 13 (1969) 1741–1747. https://doi.org/10.1002/APP.1969.070130815
Pachón-Morales J., Do H., Colin J., Puel F., Perré P., Schott D., DEM modelling for flow of cohesive lignocellulosic biomass powders: model calibration using bulk tests, Advanced Powder Technology, 30 (2019) 732–750. https://doi.org/10.1016/j.apt.2019.01.003
Packham D., Surface energy, surface topography and adhesion, International Journal of Adhesion and Adhesives, 23 (2003) 437–448. https://doi.org/10.1016/S0143-7496(03)00068-X
Palmer H.K., Rowe R.C., The application of mercury porosimetry to porous polymer powders, Powder Technology, 9 (1974) 181–186. https://doi.org/10.1016/0032-5910(74)80030-6
Park B., Min K.-B., Bonded-particle discrete element modeling of mechanical behavior of transversely isotropic rock, International Journal of Rock Mechanics and Mining Sciences, 76 (2015) 243–255. https://doi.org/10.1016/j.ijrmms.2015.03.014
Pasha M., Dogbe S., Hare C., Hassanpour A., Ghadiri M., A linear model of elasto-plastic and adhesive contact deformation, Granular Matter, 16 (2014) 151–162. https://doi.org/10.1007/s10035-013-0476-y
Paul J., Romeis S., Tomas J., Peukert W., A review of models for single particle compression and their application to silica microspheres, Advanced Powder Technology, 25 (2014) 136–153. https://doi.org/10.1016/j.apt.2013.09.009
Perkins M., Ebbens S.J., Hayes S., Roberts C.J., Madden C.E., Luk S.Y., Patel N., Elastic modulus measurements from individual lactose particles using atomic force microscopy, International Journal of Pharmaceutics, 332 (2007) 168–175. https://doi.org/10.1016/j.ijpharm.2006.09.032
Pitois O., Moucheront P., Chateau X., Liquid bridge between two moving spheres: an experimental study of viscosity effects, Journal of Colloid and Interface Science, 231 (2000) 26–31. https://doi.org/10.1006/jcis.2000.7096
Pitois O., Moucheront P., Chateau X., Rupture energy of a pendular liquid bridge, The European Physical Journal B, 23 (2001) 79–86. https://doi.org/10.1007/s100510170084
Popov V.L., Contact Mechanics and Friction—Physical Principles and Applications, Springer Berlin Heidelberg, Berlin, Heidelberg, 2017, ISBN: 9783662530801. https://doi.org/10.1007/978-3-662-53081-8
Pöschel T., Schwager T., Computational Granular Dynamics—Models and Algorithms, Springer-Verlag Berlin Heidelberg, New York, 2005, ISBN: 9783540214854. https://doi.org/10.1007/3-540-27720-X
Potapov A.V., Hunt M.L., Campbell C.S., Liquid–solid flows using smoothed particle hydrodynamics and the discrete element method, Powder Technology, 116 (2001) 204–213. https://doi.org/10.1016/S0032-5910(00)00395-8
Puderbach V., Schmidt K., Antonyuk S., A coupled CFD-DEM model for resolved simulation of filter cake formation during solid-liquid separation, Processes, 9 (2021) 826. https://doi.org/10.3390/pr9050826
Quist J., Evertsson M., Framework for DEM model calibration and validation, Proceedings of the 14th European Symposium on Comminution and Classification (ESCC), (2015) 103–108.
Rabinovich Y.I., Adler J.J., Ata A., Singh R.K., Moudgil B.M., Adhesion between nanoscale rough surfaces, Journal of Colloid and Interface Science, 232 (2000) 17–24. https://doi.org/10.1006/jcis.2000.7168
Rabinovich Y.I., Esayanur M.S., Moudgil B.M., Capillary forces between two spheres with a fixed volume liquid bridge: theory and experiment, Langmuir: the ACS Journal of Surfaces and Colloids, 21 (2005) 10992–10997. https://doi.org/10.1021/la0517639
Ramakrishna S.N., Clasohm L.Y., Rao A., Spencer N.D., Controlling adhesion force by means of nanoscale surface roughness, Langmuir: the ACS Journal of Surfaces and Colloids, 27 (2011) 9972–9978. https://doi.org/10.1021/la201727t
Reynolds G.K., Fu J.S., Cheong Y.S., Hounslow M.J., Salman A.D., Breakage in granulation: a review, Chemical Engineering Science, 60 (2005) 3969–3992. https://doi.org/10.1016/j.ces.2005.02.029

Richter C., Rößler T., Kunze G., Katterfeld A., Will F., Development of a standard calibration procedure for the DEM parameters of cohesionless bulk materials – Part II: efficient optimization-based calibration, Powder Technology, 360 (2020) 967–976. https://doi.org/10.1016/j.powtec.2019.10.052

Roessler T., Katterfeld A., DEM parameter calibration of cohesive bulk materials using a simple angle of repose test, Particuology, 45 (2019) 105–115. https://doi.org/10.1016/j.partic.2018.08.005

Roessler T., Richter C., Katterfeld A., Will F., Development of a standard calibration procedure for the DEM parameters of cohesionless bulk materials – part I: solving the problem of ambiguous parameter combinations, Powder Technology, 343 (2019) 803–812. https://doi.org/10.1016/j.powtec.2018.11.034

Rossetti D., Pepin X., Simons S.J., Rupture energy and wetting behavior of pendular liquid bridges in relation to the spherical agglomeration process, Journal of Colloid and Interface Science, 261 (2003) 161–169. https://doi.org/10.1016/S0021-9797(03)00043-2

Rotter S., Woitzik C., Düster A., Bonded particle models for discrete element simulation of porous granules, PAMM, 22 (2023) e202200164. https://doi.org/10.1002/pamm.202200164

Rudolph M., Hartmann R., Specific surface free energy component distributions and flotabilities of mineral microparticles in flotation—An inverse gas chromatography study, Colloids and Surfaces A: Physicochemical and Engineering Aspects, 513 (2017) 380–388. https://doi.org/10.1016/j.colsurfa.2016.10.069

Rumpf H., Particle Technology, Springer International Publishing; Springer Nature, Cham, 2012, ISBN: 9789401179447. https://doi.org/10.1007/978-94-011-7944-7

Sakai M., Mori Y., Sun X., Takabatake K., Recent progress on mesh-free particle methods for simulations of multi-phase flows: a review, KONA Powder and Particle Journal, 37 (2020) 132–144. https://doi.org/10.14356/kona.2020017

Santos D.A., Barrozo M.A., Duarte C.R., Weigler F., Mellmann J., Investigation of particle dynamics in a rotary drum by means of experiments and numerical simulations using DEM, Advanced Powder Technology, 27 (2016) 692–703. https://doi.org/10.1016/j.apt.2016.02.027

Schaefer D.M., Carpenter M., Gady B., Reifenberger R., Demejo L.P., Rimai D.S., Surface roughness and its influence on particle adhesion using atomic force techniques, Journal of Adhesion Science and Technology, 9 (1995) 1049–1062. https://doi.org/10.1163/156856195X00897

Schäfer J., Dippel S., Wolf D.E., Force schemes in simulations of granular materials, Journal de Physique I, 6 (1996) 5–20. https://doi.org/10.1051/JP1:1996129

Schubert H., Capillary forces—modeling and application in particulate technology, Powder Technology, 37 (1984) 105–116. https://doi.org/10.1016/0032-5910(84)80010-8

Schwarz N., Ripperger S., Antonyuk S., Investigations on the capability of the statistical extinction method for the determination of mean particle sizes in concentrated particle systems, Particle & Particle Systems Characterization, 35 (2018) 1800191. https://doi.org/10.1002/ppsc.201800191

Sereno A.M., Silva M.A., Mayor L., Determination of particle density and porosity in foods and porous materials with high moisture content, International Journal of Food Properties, 10 (2007) 455–469. https://doi.org/10.1080/10942910600880736

Sheng L.-T., Chang W.-C., Hsiau S.-S., Influence of particle surface roughness on creeping granular motion, Physical Review E, 94 (2016) 12903. https://doi.org/10.1103/PhysRevE.94.012903

Shi D., McCarthy J.J., Numerical simulation of liquid transfer between particles, Powder Technology, 184 (2008) 64–75. https://doi.org/10.1016/j.powtec.2007.08.011

Sinka I.C., Modelling powder compaction, KONA Powder and Particle Journal, 25 (2007) 4–22. https://doi.org/10.14356/kona.2007005

Slominski C., Niedostatkiewicz M., Tejchman J., Application of particle image velocimetry (PIV) for deformation measurement during granular silo flow, Powder Technology, 173 (2007) 1–18. https://doi.org/10.1016/j.powtec.2006.11.018

Soltanbeigi B., Podlozhnyuk A., Papanicolopulos S.-A., Kloss C., Pirker S., Ooi J.Y., DEM study of mechanical characteristics of multi-spherical and superquadric particles at micro and macro scales, Powder Technology, 329 (2018) 288–303. https://doi.org/10.1016/j.powtec.2018.01.082

Sommerfeld M., Huber N., Experimental analysis and modelling of particle-wall collisions, International Journal of Multiphase Flow, 25 (1999) 1457–1489. https://doi.org/10.1016/S0301-9322(99)00047-6

Staedler T., Diehl K., Fuchs R., Meyer J., Kumar A., Jiang X., Nanoindentation based colloid probe technique: a unique opportunity to study the mechanical contact of individual micron sized particles, in: Antonyuk S. (Ed.), Particles in Contact, Springer International Publishing, Cham, 2019, ISBN: 9783030158989, pp. 437–455. https://doi.org/10.1007/978-3-030-15899-6_15

Stevens A.B., Hrenya C.M., Comparison of soft-sphere models to measurements of collision properties during normal impacts, Powder Technology, 154 (2005) 99–109. https://doi.org/10.1016/j.powtec.2005.04.033

Stoianovici D., Hurmuzlu Y., A Critical study of the applicability of rigid-body collision theory, Journal of Applied Mechanics, 63 (1996) 307–316. https://doi.org/10.1115/1.2788865

Strohner D., Antonyuk S., Experimental and numerical determination of the lubrication force between a spherical particle and a microstructured surface, Advanced Powder Technology, 34 (2023) 104173. https://doi.org/10.1016/j.apt.2023.104173

Stronge W.J., Impact Mechanics, Cambridge University Press, 2010, ISBN:9780511626432. https://doi.org/10.1017/CBO9780511626432

Sutkar V.S., Deen N.G., Padding J.T., Kuipers J.A.M., Salikov V., Crüger B., Antonyuk S., Heinrich S., A novel approach to determine wet restitution coefficients through a unified correlation and energy analysis, AIChE Journal, 61 (2015) 769–779. https://doi.org/10.1002/aic.14693

Suzzi D., Toschkoff G., Radl S., Machold D., Fraser S.D., Glasser B.J., Khinast J.G., DEM simulation of continuous tablet coating: effects of tablet shape and fill level on inter-tablet coating variability, Chemical Engineering Science, 69 (2012) 107–121. https://doi.org/10.1016/j.ces.2011.10.009

Tang T., He Y., Tai T., Wen D., DEM numerical investigation of wet particle flow behaviors in multiple-spout fluidized beds, Chemical Engineering Science, 172 (2017a) 79–99. https://doi.org/10.1016/j.ces.2017.06.025

Tang Y., Kuipers J.A.M., Buck B., Heinrich S., Deen N.G., Interface-resolved simulations of normal collisions of spheres on a wet surface, AIChE Journal, 63 (2017b) 4774–4787. https://doi.org/10.1002/aic.15847

Tardos G.I., Khan M.I., Mort P.R., Critical parameters and limiting conditions in binder granulation of fine powders, Powder Technology, 94 (1997) 245–258. https://doi.org/10.1016/S0032-5910(97)03321-4

Tavares L.M., A Review of advanced ball mill modelling, KONA Powder and Particle Journal, 34 (2017) 106–124. https://doi.org/10.14356/kona.2017015

Thakur S.C., Morrissey J.P., Sun J., Chen J.F., Ooi J.Y., Micromechanical analysis of cohesive granular materials using the discrete element method with an adhesive elasto-plastic contact model, Granular Matter, 16 (2014) 383–400. https://doi.org/10.1007/s10035-014-0506-4

Thornton C., Cummins S.J., Cleary P.W., On elastic-plastic normal contact force models, with and without adhesion, Powder Technology, 315 (2017) 339–346. https://doi.org/10.1016/j.powtec.2017.04.008

Thornton C., Ning Z., A theoretical model for the stick/bounce behaviour of adhesive, elastic-plastic spheres, Powder Technology, 99 (1998) 154–162. https://doi.org/10.1016/S0032-5910(98)00099-0

Tomas J., Adhesion of ultrafine particles—A micromechanical approach, Chemical Engineering Science, 62 (2007a) 1997–2010. https://doi.org/10.1016/j.ces.2006.12.055

Tomas J., Adhesion of ultrafine particles—Energy absorption at contact, Chemical Engineering Science, 62 (2007b) 5925–5939. https://doi.org/10.1016/j.ces.2007.06.036

Tsotsas E., Mujumdar A.S., Modern Drying Technology, Wiley, 2011, ISBN: 9783527631636.

Tsuji Y., Discrete particle simulation of gas-solid flows (From dilute to dense flows), KONA Powder and Particle Journal, 11 (1993) 57–68. https://doi.org/10.14356/kona.1993010

Tsuji Y., Tanaka T., Ishida T., Lagrangian numerical simulation of plug flow of cohesionless particles in a horizontal pipe, Powder Technology, 71 (1992) 239–250. https://doi.org/10.1016/0032-5910(92)88030-L

Tykhoniuk R., Tomas J., Luding S., Kappl M., Heim L., Butt H.-J., Ultrafine cohesive powders: from interparticle contacts to continuum behaviour, Chemical Engineering Science, 62 (2007) 2843–2864. https://doi.org/10.1016/j.ces.2007.02.027

Vångö M., Pirker S., Lichtenegger T., Unresolved CFD–DEM modeling of multiphase flow in densely packed particle beds, Applied Mathematical Modelling, 56 (2018) 501–516. https://doi.org/10.1016/j.apm.2017.12.008

Vollmari K., Jasevičius R., Kruggel-Emden H., Experimental and numerical study of fluidization and pressure drop of spherical and non-spherical particles in a model scale fluidized bed, Powder Technology, 291 (2016) 506–521. https://doi.org/10.1016/j.powtec.2015.11.045

Walton O.R., Braun R.L., Viscosity, granular-temperature, and stress calculations for shearing assemblies of inelastic, frictional disks, Journal of Rheology, 30 (1986) 949–980. https://doi.org/10.1122/1.549893

Washino K., Chan E.L., Midou H., Tsuji T., Tanaka T., Tangential viscous force models for pendular liquid bridge of Newtonian fluid between moving particles, Chemical Engineering Science, 174 (2017) 365–373. https://doi.org/10.1016/j.ces.2017.09.028

Washino K., Chan E.L., Tsujimoto T., Tsuji T., Tanaka T., Development of resolved CFD–DEM coupling model for three-phase flows with non-spherical particles, Chemical Engineering Science, 267 (2023) 118335. https://doi.org/10.1016/j.ces.2022.118335

Weir G., Tallon S., The coefficient of restitution for normal incident, low velocity particle impacts, Chemical Engineering Science, 60 (2005) 3637–3647. https://doi.org/10.1016/j.ces.2005.01.040

Weis D., Grohn P., Evers M., Thommes M., García E., Antonyuk S., Implementation of formation mechanisms in DEM simulation of the spheronization process of pharmaceutical pellets, Powder Technology, 378 (2021) 667–679. https://doi.org/10.1016/j.powtec.2020.09.013

Weis D., Krull F., Mathy J., Evers M., Thommes M., Antonyuk S., A contact model for the deformation behaviour of pharmaceutical pellets under cyclic loading, Advanced Powder Technology, 30 (2019) 2492–2502. https://doi.org/10.1016/j.apt.2019.07.026

Wittel F.K., Mani R., Melnikov K., Bianchi F., Herrmann H.J., Capillary interaction in wet granular assemblies: part 2, in: Antonyuk S. (Ed.), Particles in Contact, Springer International Publishing, Cham, 2019, ISBN: 9783030158989, pp. 277–309. https://doi.org/10.1007/978-3-030-15899-6_9

Wolff M., Salikov V., Antonyuk S., Heinrich S., Schneider G.A., Three-dimensional discrete element modeling of micromechanical bending tests of ceramic–polymer composite materials, Powder Technology, 248 (2013) 77–83. https://doi.org/10.1016/j.powtec.2013.07.009

Wu M., Khinast J.G., Radl S., The effect of liquid bridge model details on the dynamics of wet fluidized beds, AIChE Journal, 64 (2018) 437–456. https://doi.org/10.1002/aic.15947

Xiao F., Jing J., Kuang S., Yang L., Yu A., Capillary forces on wet particles with a liquid bridge transition from convex to concave, Powder Technology, 363 (2020) 59–73. https://doi.org/10.1016/j.powtec.2020.01.020

Ye Y., Zeng Y., A size-dependent viscoelastic normal contact model for particle collision, International Journal of Impact Engineering, 106 (2017) 120–132. https://doi.org/10.1016/j.ijimpeng.2017.03.020

Zhang T., Zhang C., Zou J., Wang B., Song F., Yang W., DEM exploration of the effect of particle shape on particle breakage in granular assemblies, Computers and Geotechnics, 122 (2020) 103542. https://doi.org/10.1016/j.compgeo.2020.103542

Zhao B., Wang J., 3D quantitative shape analysis on form, roundness, and compactness with μCT, Powder Technology, 291 (2016) 262–275. https://doi.org/10.1016/j.powtec.2015.12.029

Zhou H., Götzinger M., Peukert W., The influence of particle charge and roughness on particle–substrate adhesion, Powder Technology, 135-136 (2003) 82–91. https://doi.org/10.1016/j.powtec.2003.08.007

Zhu H.P., Zhou Z.Y., Yang R.Y., Yu A.B., Discrete particle simulation of particulate systems: theoretical developments, Chemical Engineering Science, 62 (2007) 3378–3396. https://doi.org/10.1016/j.ces.2006.12.089

Authors' Short Biographies

Fabian Krull received his master's degree in chemical engineering from the University of Dortmund in 2015. Since January 2016, he has been working at the Institute of Particle Process Engineering at the University of Kaiserslautern-Landau (RPTU). His research projects focus on particle micromechanism during collisions, taking topography into account, mechanical behavior of bio-cell agglomerates, Discrete Element Method simulations coupled with CFD, and the development of measurement methods for determining contact model parameters.

David Strohner received his B.Sc. in process engineering from the University of Applied Sciences Mannheim in 2016 and continued his studies in energy and process engineering at the University of Kaiserslautern, where he received his M.Sc. in 2019. Since 2020, he has been working as a PhD student at the Institute of Particle Process Engineering at the RPTU Kaiserslautern-Landau, with a focus on particle dynamics under the influence of liquids as well as numerical simulations of particle processes.

Prof. Sergiy Antonyuk is the director of the Institute of Particle Process Engineering at the University of Kaiserslautern-Landau (RPTU), Germany. He studied Process Equipment and Engineering at TU Donetsk, Ukraine, and earned his first PhD in ecological safety at TU Kyiv in 2004. In 2006, he completed his second PhD in Process Engineering at the University of Magdeburg under the guidance of Prof. Jürgen Tomas. After working as a Junior-Professor at TU Hamburg in 2008–2014, he became a full professor at RPTU. His research focuses on contact mechanics, particle breakage dynamics, powder flow behavior, filtration, aerosol technology, and multiphase flow simulations.